

ARTICLE

Received 19 May 2016 | Accepted 28 Dec 2016 | Published 15 Feb 2017

DOI: 10.1038/ncomms14423

OPEN

# Haploinsufficiency networks identify targetable patterns of allelic deficiency in low mutation ovarian cancer

Joe Ryan Delaney<sup>1</sup>, Chandni B. Patel<sup>1</sup>, Katelyn McCabe Willis<sup>1</sup>, Mina Haghghiabyaneh<sup>1</sup>, Joshua Axelrod<sup>1</sup>, Isabelle Tancioni<sup>1</sup>, Dan Lu<sup>1</sup>, Jaidev Bapat<sup>1</sup>, Shanique Young<sup>1</sup>, Octavia Cadassou<sup>1,2</sup>, Alena Bartakova<sup>1</sup>, Parthiv Sheth<sup>1</sup>, Carley Haft<sup>1</sup>, Sandra Hui<sup>1</sup>, Cheryl Saenz<sup>1</sup>, David D. Schlaepfer<sup>1</sup>, Olivier Harismendy<sup>3</sup> & Dwayne G. Stupack<sup>1</sup>

Identification of specific oncogenic gene changes has enabled the modern generation of targeted cancer therapeutics. In high-grade serous ovarian cancer (OV), the bulk of genetic changes is not somatic point mutations, but rather somatic copy-number alterations (SCNAs). The impact of SCNAs on tumour biology remains poorly understood. Here we build haploinsufficiency network analyses to identify which SCNA patterns are most disruptive in OV. Of all KEGG pathways ( $N=187$ ), autophagy is the most significantly disrupted by coincident gene deletions. Compared with 20 other cancer types, OV is most severely disrupted in autophagy and in compensatory proteostasis pathways. Network analysis prioritizes *MAP1LC3B* (*LC3*) and *BECN1* as most impactful. Knockdown of *LC3* and *BECN1* expression confers sensitivity to cells undergoing autophagic stress independent of platinum resistance status. The results support the use of pathway network tools to evaluate how the copy-number landscape of a tumour may guide therapy.

<sup>1</sup>Division of Gynecologic Oncology, Department of Reproductive Medicine, UCSD School of Medicine and UCSD Moores Cancer Center, 3855 Health Sciences Drive, La Jolla, California 92037, USA. <sup>2</sup>Centre de recherche en Cancérologie, INSERM 1052, CNRS 5286, Centre Léon Bérard, Université de Lyon, Lyon, France. <sup>3</sup>Division of Biomedical Informatics, Department of Medicine, UCSD School of Medicine and UCSD Moores Cancer Center, 3855 Health Sciences Drive, La Jolla, California 92093, USA. Correspondence and requests for materials should be addressed to J.R.D. (email: jrdelaney@ucsd.edu) or to D.G.S. (email: dstupack@ucsd.edu).

Characterization of specific cancer mutations has yielded a map of which oncogenes and tumour suppressors that may be chemically or biologically targetable<sup>1,2</sup> and guided immunotherapy<sup>3</sup>. However, single-nucleotide variants and short insertion–deletion mutations (here referred to simply as ‘mutations’) are not the sole drivers of oncogenesis. High-grade serous ovarian cancer (OV) is uniquely low in mutation and high in somatic copy-number alterations (SCNAs). SCNAs drive cancer through losses of tumour suppressors or amplifications of oncogenes, often by large SCNAs encompassing hundreds of genes<sup>4</sup>.

Homozygous deletion occurs rarely (1–2% of SCNAs) due to co-deletion of essential genes. On a gene-to-gene basis, SCNAs are more common than mutations even in highly mutated cancer types and ~95% of SCNAs observed in tumours are monoallelic changes. However, with ~16,000 genes with SCNAs in the average OV tumour (Fig. 1d), statistical modelling of driver SCNAs is complicated by pervasive ‘background’ SCNAs, which may not drive tumour progression. Previous analyses of SCNAs via chromosome arm alterations identified correlated pairs<sup>5,6</sup>, but lack a consideration of collaborative monoallelic SCNAs altering entire molecular pathways. Pathway analysis can improve an understanding of which molecular processes are altered when multiple genes contribute to cellular function, since different gene deletion combinations can yield identical phenotypes.

We developed a new tool to analyse highly variable SCNA tumours to determine significantly altered pathways and the gene-level SCNAs, which most likely contribute to pathway disruption. The tool is designed to incorporate known pathway concepts of genetic bottlenecks<sup>7</sup>, and is found to correctly prioritize known tumour suppressors and oncogenes as impactful genes in OV. By this analysis, the most suppressed pathway in OV is autophagy. Many other proteostasis pathways, such as the proteasome, endoplasmic reticulum (ER) stress and the lysosome are suppressed in OV. In validation of these computational findings, treatment of multiple OV *in vivo* models

by autophagy- and proteostasis-disrupting drugs abolishes tumour growth. Knockdown of *BECN1* and *LC3B* sensitizes OV to the autophagy halting drug chloroquine. These results implicate autophagy as a major disrupted pathway in OV, which is also amenable to therapy.

## Results

**Half of ovarian tumours lack clear driver mutations.** OV tumours have been characterized<sup>8</sup> as being uniquely low in mutations and high in SCNAs (Fig. 1a). However, it is possible that despite relatively low mutation rates, each OV tumour nonetheless contains multiple tumour suppressor or oncogene mutations that drive cancer formation. To investigate this possibility, we analysed The Cancer Genome Atlas (TCGA) OV data for mutations in well-known tumour-driver genes<sup>8</sup>. Interestingly, 48% of studied tumours have no mutations in these oncogenes or tumour suppressors, other than *TP53* (Fig. 1b). Since mutant p53 alone is insufficient for tumour formation<sup>9,10</sup>, these tumours likely contain SCNA drivers<sup>5</sup> which aid in tumorigenesis. Given the high ratio of SCNAs to mutations in OV (Fig. 1c,d), we sought a new method to better understand potential SCNA drivers.

**Design of the HAPTRIG SCNA analysis tool.** We developed a computational tool to identify pathways significantly disrupted by SCNAs in the highly noisy genetic background of OV tumours. The program was designed to analyse diverse genetic backgrounds which all yield at least one similar phenotype (Fig. 2a). Many biological pathways have multiple bottleneck<sup>7</sup> or regulatory points<sup>11</sup>, any of which can equivalently affect pathway phenotype<sup>12</sup>. While Gene Set Enrichment Analysis (GSEA) also looks at multiple genes within a pathway to determine statistical significance at the cohort level<sup>13</sup>, we designed our tool to incorporate two additional pieces of information to better characterize genetic disturbance of pathway biology:

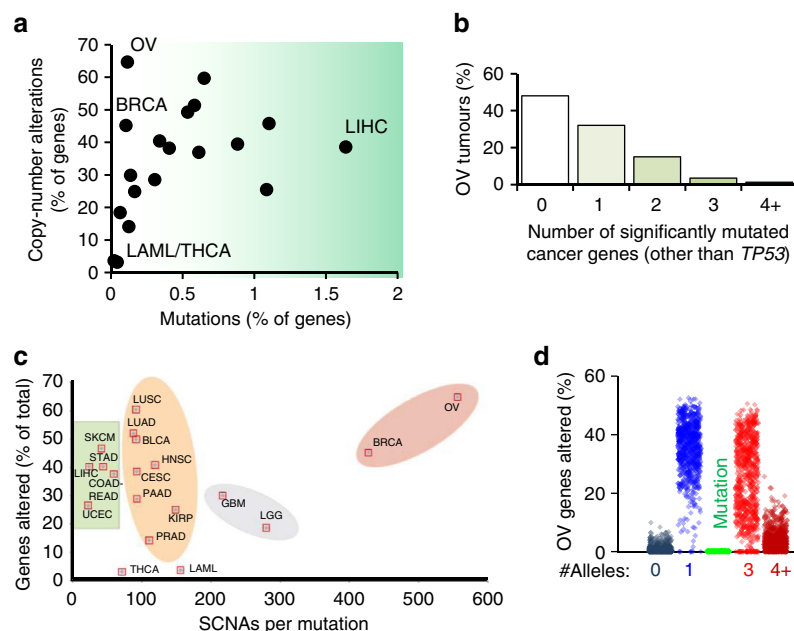


**Figure 1 | Prevalence of gene-level alterations in cancer.** (a) The average percentage of genes with either somatic copy-number alterations (SCNAs) or somatic point and small indel mutations for TCGA studied cancers ( $N = 9,740$  tumors). (b) The number of significantly mutated cancer genes<sup>8</sup> other than TP53 that are mutant in OV is plotted as a percentage of primary tumours from TCGA studied patients. Nearly half have no oncogenic mutation other than TP53. (c) Ratio of SCNAs to mutations relative to total percentage of genes changed across cancer types. (d) The percent of genes altered by either SCNA (allele numbers 0, 1, 3 or 4+) or by mutation is plotted for each TCGA OV tumour ( $N = 579$  for SCNAs,  $N = 316$  for mutations).

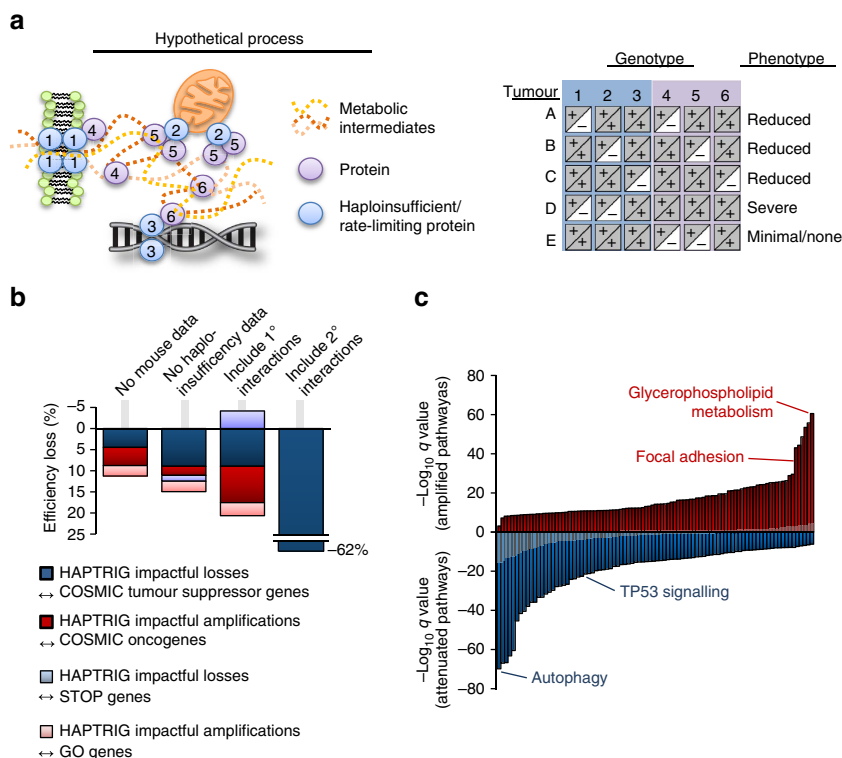


**Figure 2 | Design of HAPTRIG and OV pan-pathway analysis.** (a) Schematic of the rationale behind designing HAPTRIG network analyses. Genotypes with similar phenotypes can be spread across many genes and each tumour may alter the phenotype using different genes. Haploinsufficient genes are more likely to drive phenotype changes, as are highly interactive genes. (b) Different versions of HAPTRIG were coded and executed to test which inputs prioritized genes with known tumour suppressor or oncogenic function, as annotated in COSMIC, and for ability to prioritize ‘STOP’ and ‘GO’ genes as expected. HAPTRIG was most effective across all KEGG pathways when considering protein–protein interactions within pathway genes only and when mouse and/or yeast orthologue haploinsufficiency data were included. Including genes that interacted with pathway genes (1° interactors) reduced efficiency as did including genes with an additional interaction distance from pathway genes (2° interactors). (c) HAPTRIG network analyses were created for all distinct, human KEGG pathways ( $N = 187$  pathways) and significantly disrupted pathways are plotted by significance compared with a minimally altered SCNA cancer type, thyroid cancer (THCA; in grey overlay). The top-disrupted pathways are noted in comparison with known canonical OV-disrupted pathways, focal adhesion and p53 signalling. Detailed information on these pathways is in Supplementary Data 1, and secondary OV data sets can be found in Supplementary Data 2 and 3.

protein–protein interactions (to prioritize genes that modulate other genes within the same pathway) and haploinsufficiency data (to prioritize genes that are known to affect biology when only a single gene copy is altered).

This Haploinsufficient/Triplosensitive Gene (HAPTRIG) tool generates network scores by (1) building protein–protein interaction networks of pathway proteins from BioGRID<sup>14</sup>, (2) prioritizing interactions that contain a haploinsufficient or triplosensitive gene, (3) negatively scoring interactions containing gene deletion SCNAs and positively scoring interactions containing gene amplification SCNAs, and (4) summing all interaction scores within a molecular pathway. For statistical significance, pathway scores from observed tumours were compared with control data of 1000 tumour-paired randomly permuted SCNAs to derive a  $P$  value of observed tumour pathway changes compared with what would be expected by chance (for a schematic, see Supplementary Fig. 1). This design enables statistically significant pathway changes in a cohort of tumours to be detected in a high noise background. In addition, the HAPTRIG pipeline scores the contribution of each gene within a pathway to allow for ranking the biological importance of each gene within a pathway. For example, since *TP53* is highly interactive and often deleted, it is ranked by the HAPTRIG tool as the most impactful deletion within the p53 pathway for most OV tumours.

To test the robustness of the HAPTRIG approach, we queried HAPTRIG for its ability to prioritize known tumour suppressor genes and oncogenes<sup>15</sup>, as most affecting deleted or amplified gene sets, respectively, and similarly tested for ‘STOP’ and ‘GO’ gene<sup>4</sup> prioritization. Using the full HAPTRIG approach as a reference, we measured how its sensitivity is affected by the following parameters: (1) removal of haploinsufficient orthologue data from mice and yeast, (2) inclusion of only intrinsic (within gene set only) interactions or primary/secondary interactions as well, and (3) when gene ontology (GO) pathways were used in place of comparable Kyoto Encyclopedia of Genes and Genomes (KEGG) pathways (Fig. 2b, Supplementary Fig. 2A). All components altered HAPTRIG efficiency in the range of 10–60%. While we predict many GO pathways to be useful in HAPTRIG analysis, GO pathways are typically much larger and contain many genes with tangential relation to core pathway function. The most accurate view of SCNA-altered pathways within OV was thus found by using all distinct, human KEGG pathways ( $N = 187$  pathways) scored for intrinsic and haploinsufficient interactions.

**HAPTRIG pathway analysis of OV identifies autophagy loss.** In TCGA OV cohort, we observed the most statistically unlikely disrupted deletion-enriched pathway to be autophagy

(followed by FoxO signalling, adipocytokine signalling, arginine/proline metabolism and NOTCH signalling) and the most statistically unlikely disrupted amplification-enriched pathway to be glycerophospholipid metabolism (Fig. 2c, all disrupted pathway data in Supplementary Data 1). Known altered pathways such as p53 and focal adhesion were also significantly altered, albeit at lower significance. This pattern persisted in an independent OV cohort<sup>16</sup> but did not reach statistical significance in an endometrioid OV cohort, perhaps due to small sample size (Supplementary Fig. 2; Supplementary Data 2 and 3). While we focus on KEGG pathways here, HAPTRIG functions on any pathway set (Hallmark pathway set results shown in Supplementary Data 4). HAPTRIG improves on GSEA to identify these significantly disrupted pathways: only two KEGG pathways reached statistical significance using GSEA (Supplementary Table 1; Supplementary Fig. 3). We release the code for HAPTRIG as Supplementary Software 1, and provide example input data sets as Supplementary Data 5.

Autophagy has long been implicated in tumour development and may have dual roles: loss of autophagy genes including *BECN1* leads to early oncogenesis in mouse models<sup>17,18</sup>; however, *KRAS* mutant cancers are addicted to elevated autophagy<sup>19</sup>. Interestingly, most proteostasis pathways in our pan-pathway analysis were enriched for deletions, including ER stress, ubiquitin-mediated proteolysis and the lysosome, although the peroxisome pathway was enriched for amplifications. Haploinsufficiency in model organism screens is associated with an inability to form adequately proportioned protein-quality control complexes<sup>20</sup>, suggesting single allele SCNAs disrupt these pathways. To determine whether proteostasis disruption was specific to OV, we ran HAPTRIG analyses across 20 other cancer types studied by TCGA. Alterations ranged from minimal among acute myeloid leukaemia and thyroid cancers, a strongly suppressed network of proteostasis genes in invasive breast (BRCA) and serous ovarian (OV) cancers, to a uniquely amplified autophagy network in renal papillary cell carcinoma (KIRC; Fig. 3a). Many genes were frequently altered in OV, and HAPTRIG ranked known biologically impactful genes (for example, *BRCA1*, *TP53*, *BECN1* and *CASP3*) as most altered for OV (Fig. 3b, full OV networks in Supplementary Fig. 4), as well as some genes uncommonly associated with cancer (for example, *CTSD* for lysosomal function and *PEX5* for peroxisomal function, full summary in Supplementary Table 2). OV was clearly the most disrupted for proteostasis amongst these 21 tumour types. We next evaluated whether these SCNA network alterations contribute to cancer phenotypes as mutations do, and whether they might be predictably targeted.

### Targeting autophagy and proteostasis *in vivo* halts OV growth.

Well-controlled single-allele losses reduce messenger RNA (mRNA) expression up to 90% of the time, even in a single unstressed experimental condition<sup>21</sup>. In OV, protein expression correlated with mRNA expression for 80–90% of genes<sup>22</sup>. Autophagy depends on mRNA induction for full function<sup>23</sup>. TCGA OV tumours exhibit decreased mRNA expression of core autophagy genes upon heterozygous loss and often contain several core autophagy gene deletions (Supplementary Fig. 5). Such pervasive deletions in protein and organelle quality control genes may sensitize OV to proteotoxic, autophagy-stressing drugs<sup>24</sup>; redundant losses may underlie the severely compromised capacity of these tumours to compensate for proteotoxic treatment combinations (Supplementary Fig. 6). To investigate this possibility, we treated OVCAR3 cells with chloroquine, to prevent autophagy resolution<sup>25</sup>, and nelfinavir, to

promote ER stress<sup>26</sup>. Protein aggregates increased by 3–6-fold (Supplementary Fig. 7), concurrent with the accumulation of autophagolysosomes (Supplementary Fig. 8). The phenotype was further amplified when chloroquine/nelfinavir was combined with rapamycin and/or dasatinib<sup>24</sup>, which we term Combination Of Autophagy Selective Therapeutics (COAST; Supplementary Fig. 8). Proteasomal inhibitors also stress autophagy, and bortezomib exhibited cytotoxicity in the low nanomolar range. However, bortezomib was not OV selective and risks high clinical toxicity (Supplementary Fig. 9). Cytotoxic concentrations required for the OV tumour cells were low for other proteostasis-targeting agents (Supplementary Figs 10 and 11). Chloroquine and nelfinavir within the concentration range found in patients' blood<sup>24</sup> was sufficient to prevent single-cell colony formation, cell growth in suspension, and to promote cytotoxicity (Supplementary Fig. 12) in OV cells. Higher-order combinations (COAST) were selective across six different OV tumour cell lines (Supplementary Fig. 11) with autophagy gene deletions (Supplementary Table 3), and no drug or combination reduced the effects of any other drug.

We next evaluated whether this HAPTRIG-informed choice of drugs would ameliorate disease in preclinical models of OV. Cisplatin and docetaxel did not alter the growth of a patient-derived xenograft model derived from a recurrent chemotherapy-resistant patient (Fig. 4a), while the proteostasis-targeted cocktail resulted in a striking complete ablation of tumour growth. Given the lack of any macroscopic disease, we next used an ID8-IP-mCherry labelled tumour model<sup>27</sup> to allow detection of persistent microscopic disease. Again, mice treated with COAST showed eradication of tumours, although microscopic nests of cells were still detected in 2/8 mice. Interestingly, chloroquine and nelfinavir alone did not result in statistically significant inhibition (Fig. 4b), despite having the best efficacy of two drugs *in vitro* (Supplementary Fig. 10), possibly reflecting the complexity of the tumour microenvironment and other forms of heterogeneity in syngeneic models. This five drug cocktail was remarkably well tolerated in mice<sup>24</sup>, in which we tested up to 8 weeks of COAST therapy, long after all control mice perished (Supplementary Fig. 13). COAST also arrested tumour growth in a subcutaneous OVCAR3 model (Fig. 4c), with residual tumour showing accumulation of autophagosomal Lc3-II and the ER stress marker Grp78 (Fig. 4d).

**Impactful HAPTRIG genes influence OV drug targeting.** Since genetic targeting is an important consideration of new therapies, we next utilized HAPTRIG network information to determine gene SCNAs most likely to have an impact on autophagy in OV. These most 'impactful' genes were identified by summing the score contribution of each gene within HAPTRIG networks across all tumours. We ranked impactful suppressive and oncogenic genes for all pathways in OV (Supplementary Table 2). For autophagy, the two highest impact genes were *MAP1LC3B* (*LC3*) and *BECN1*. These two genes were also commonly lost in OV, along with *ATG10*, *ULK2* and *GAPARAPL2* (Fig. 5a). *LC3* and/or *BECN1* are monoallelically deleted in 94% of OV (Supplementary Fig. 5C). Mechanistically, this may explain the sensitivity of OV tumours to drugs pressuring the autophagy network, since orthologues of each gene confer haploinsufficiency in yeast<sup>20</sup> or mice<sup>18</sup>. These losses occur early in the evolution of OV<sup>28</sup> and have an associated defect in expression when monoallelically lost (Supplementary Fig. 5), consistent with previous reports<sup>29</sup>. OV cell lines that differ in *LC3* and *BECN1* gene dose (Fig. 5b) were next tested for differences in autophagy.

OVCAR3 is a cisplatin-resistant tumour cell genetically similar to TCGA assayed OV<sup>30</sup>, exhibiting monoallelic deletions

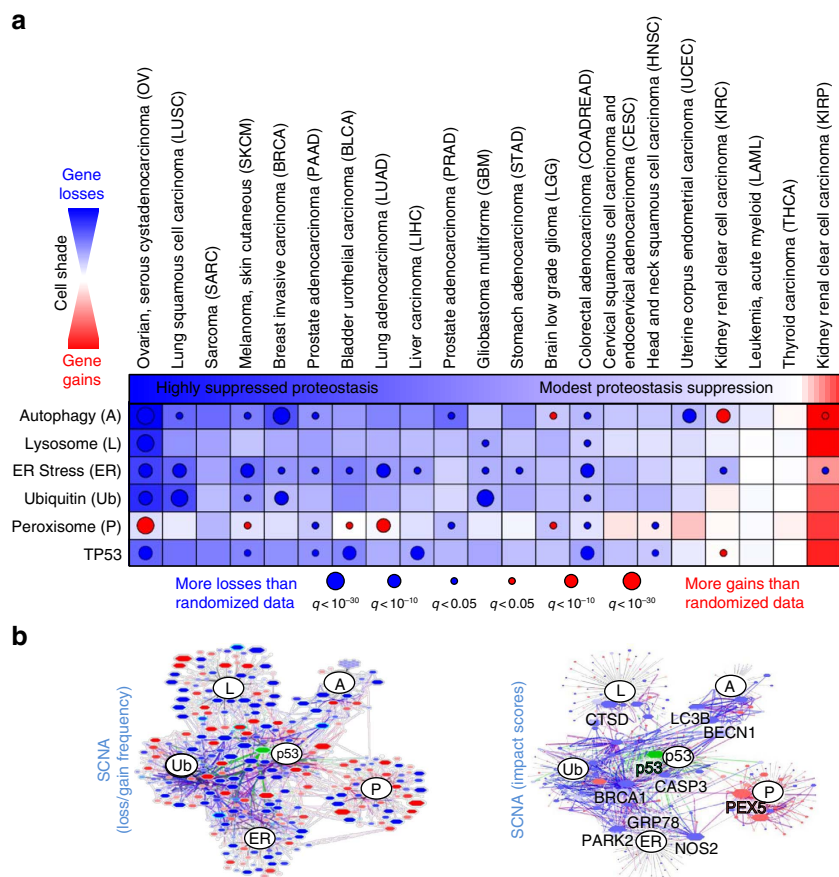


**Figure 3 | Summary of HAPTRIG proteostasis network scores across 21 cancer types.** (a) HAPTRIG analyses were performed for proteostasis pathways and the p53 pathway. Since these pathways are functionally interdependent, HAPTRIG scored both intrinsic and primary interactions from within these different pathways. The chart displays pathway network scores as blue fill if deletion-enriched, red fill if gain-enriched, and white fill for neither. Significance is represented as overlaid circles of size proportional to the  $\log_{10} q$  value. (b) OV HAPTRIG networks were visually graphed by Cytoscape, with gene node and edge protein-protein interaction size proportional to the penetrance of the gene changes within the cancer type (left panel) or by HAPTRIG predicted gene-impact scores (right panel). A red fill is assigned if the majority of copy-number changes are positive, and blue if they are negative. Node outlines are highlighted in cyan if haploinsufficiency annotations are associated with that gene. Green fill and edges indicate genes mutated in  $>10\%$  of the tumour cohort. Expanded HAPTRIG OV networks, with gene labels, are available in Supplementary Fig. 3.

of *LC3* and *BECN1*, and forming appropriate high-grade histology in mice<sup>31</sup>. In contrast, IGROV1 and SKOV3 are characterized as ovarian, but not serous (nor high SCNA) ovarian, cancer<sup>30</sup> cell lines that have lost neither allele (Fig. 5b). Flux through autophagy showed a delayed response in OVCAR3 relative to IGROV1 and SKOV3 following treatment with chloroquine, as measured using complementary assays (Fig. 5c,d)<sup>25,32</sup>. Similar results were found when autophagy was perturbed with rapamycin, nelfinavir or combination (COAST) treatments (Supplementary Fig. 14). While few OV cell lines are currently well established and also contain common OV genetics<sup>31,33,34</sup>, we additionally studied OVCAR5, OVCAR8, the patient-derived xenograft model cells LPPDOV and A2780 for autophagic response to chloroquine and again found cell lines with low HAPTRIG scores to poorly induce autophagy upon chloroquine stress (Supplementary Fig. 15), which correlated with increased cell death. Taken together, although OV cells are not completely lacking autophagy, a maximized response to stress is compromised among cells with losses in autophagy genes such as *LC3* and *BECN1*.

To test directly whether suppression of *LC3/BECN1* was sufficient to confer a proteostasis bottleneck, we next evaluated IGROV1 or SKOV3 cells stably expressing lentiviral

shRNA selected for modest suppression ( $\sim 35\text{--}70\%$ ) of *LC3* or Beclin. Slowed autophagosome accumulation was clearly observed with *shLC3*, although not significantly with *shBECN1* (Fig. 5e,f). Cells with reduced *LC3* or *BECN1* showed compromised survival following treatment with chloroquine, which prevents clearance of autophagosomes<sup>35</sup> (Fig. 5g). This survival defect was observed with multiple cell types, including IGROV1 and a glioblastoma (U373) resistant to autophagy drugs (Supplementary Figs 10 and 16). Resistance to cisplatin, a standard of care agent used to treat OV, was not indicative of response to COAST drugs including chloroquine (Fig. 5g; Supplementary Figs 10 and 15). Rather, autophagy-stressing drugs compromised cell survival selectively among lines with autophagy gene losses, regardless of single or combined drug treatment (Supplementary Figs 10, 11 and 15). The results support a model implicating haploinsufficiency, at a minimum for *LC3* and *BECN1*, in the sensitivity of OV to agents targeting autophagy.

## Discussion

The HAPTRIG tool represents an initial haploinsufficiency network-based analysis program that can be applied genome

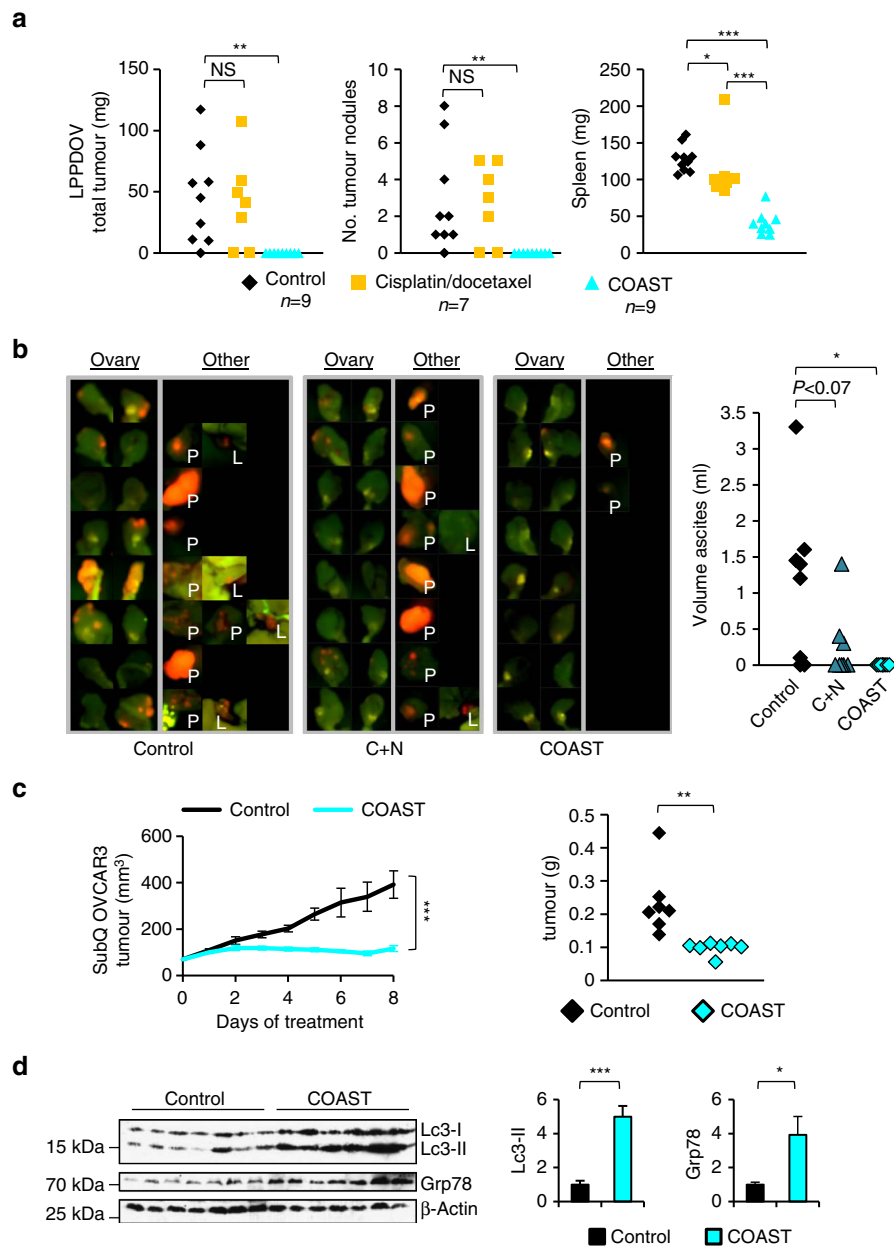


**Figure 4 | OV tumours are sensitive to disruption of proteostasis. (a)** Low passage patient-derived OV (LPPDOV) ascites cells from a patient who failed cisplatin–docetaxel chemotherapy were injected i.p. into Nu/nu mice, allowed to disseminate and grow for 10 days, and then treated with control 50% PEG400 or with COAST (Combination of Autophagy Selective Therapeutics: chloroquine  $30 \text{ mg kg}^{-1}$ , nelfinavir  $250 \text{ mg kg}^{-1}$ , rapamycin  $2.24 \text{ mg kg}^{-1}$ , dasatinib  $4 \text{ mg kg}^{-1}$  and metformin  $150 \text{ mg kg}^{-1}$  in 50% PEG400) daily for 15 days. An additional control group was treated with cisplatin/docetaxel chemotherapy (injected i.p. with  $1 \text{ mg kg}^{-1}$  cisplatin and  $2.5 \text{ mg kg}^{-1}$  docetaxel once per week starting at the first control treatment day for 2 weeks). Upon harvest, all visible and palpable tumours in the peritoneum space were dissected, counted and weighed, as were mouse spleens. **(b)** C57BL/6 immunocompetent mice were injected i.p. with ID8-IP-mCherry cells ( $N = 8$  per group). After 2 weeks to permit tumour establishment, mice were orally gavaged daily with control 50% PEG400, with COAST, or chloroquine and nelfinavir alone. At 14 days, control mice developed ascites. All groups were killed, ascites were measured and tumour burden assayed by native mCherry fluorescence. Ovaries are displayed for all mice, and any additional tumor fluorescence observed is displayed on the right panel with labels ‘P’ for peritoneal wall growth and ‘L’ for liver. **(c)** Nu/nu mice with  $100 \text{ mm}^3$  subcutaneous OVCAR3 tumours were gavaged with COAST or control and tumour growth monitored by digital calipers for 7 days. Tumours were then dissected, weighed and **(d)** subjected to immunoblotting for autophagosomal Lc3-II and the ER stress marker Grp78 (mean  $\pm$  s.e.m.  $N = 7$  mice per group).  $*P < 0.05$ ,  $**P < 0.01$ ,  $***P < 0.001$  by Wilcoxon rank-sum test.

wide for any cancer. Sequencing of mutations has identified potentially targetable genes in minorities of OV patients<sup>34,36</sup>. However, given the excessive (two-third of the genome) SCNAs present in OV (Fig. 1a–d), we undertook a strategy to identify pathways that are uniquely and perhaps unexpectedly

disrupted by SCNAs. Our permutation strategy enabled identification of significant pathways despite a potentially passenger-filled SCNA landscape. Critically, aside from merely identifying known altered genetics such as suppression of the p53 pathway, enhancement of the focal adhesion pathway

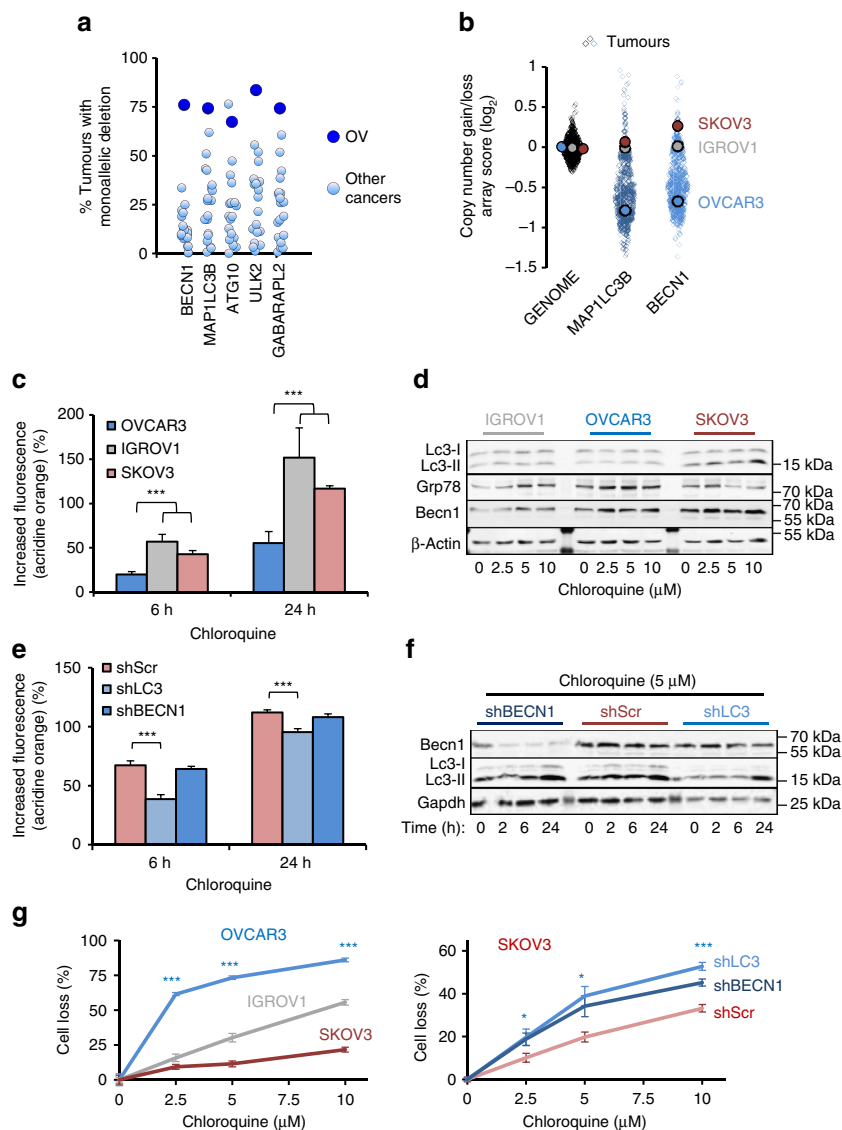


**Figure 5 | Suppression of LC3 and BECN1 lowers cellular capacity to overcome proteotoxicity.** (a) The five genes most lost in the autophagy KEGG pathway in OV compared with 20 other cancers in tumour gene loss prevalence. (b) Log<sub>2</sub> SNP6 array scores for each tumour in OV compared with three OV cell lines. 'Genome' corresponds to the average gene score for an individual tumour. OVCAR3 is the most established OV cell line with high-grade serous genetics<sup>30</sup>, whereas IGROV1 and SKOV3 are ovarian cancer cell lines without serous OV genetics. (c) OVCAR3 has delayed accumulation of acidic vacuoles including autophagosomes and lysosomes, as measured by acridine orange flow cytometry, when treated with the autophagy/lysosome inhibitor chloroquine (10  $\mu$ M). Data represent the mean  $\pm$  s.e.m. from four independent experiments. Note that additional cell lines are tested in Supplementary Fig. 15. (d) Western blots of autophagosomal Lc3-II indicate reduced accumulation of autophagosomes in OVCAR3 and increased levels of ER stress marker Grp78 when treated with chloroquine. Lysates from three independent experiments were analysed and a representative blot is shown. (e) SKOV3 cells knocked down by BECN1 and LC3 shRNA were treated with 10  $\mu$ M chloroquine for the indicated times. Only shLC3 showed reduced accumulation of autophagosomes by flow cytometric reading of acridine orange stain. Data represent the mean and s.e.m. from four independent experiments. (f) Western blots of cells treated as in e, showing reduced Lc3-II accumulation only in shLC3 cells. Lysates from three independent experiments were analysed and a representative blot is shown. (g) OV cells were treated with chloroquine for 48 h at the doses indicated and stained for cell loss by crystal violet. Data represent the mean  $\pm$  s.e.m. from eight independent experiments. \* $P$  < 0.05, \*\*\* $P$  < 0.001 by two-tailed Student's  $t$ -test.

and disruption of homologous recombination repair pathways<sup>37</sup>, our top hits are not currently considered to be canonical OV driver pathways. Yet, using *in vivo* and *in vitro* models, we validated that autophagy was suppressed in OV and moreover that by targeting this suppression by drugs that disrupt proteostasis we achieved remarkable tumour remission independent of platinum resistance.

Given the strong autophagy phenotypes we found in OV, it is curious why the autophagy pathway has not been emphasized in prior integrative analysis publications. Previous publications have

supported the finding that OV is deficient in DNA repair pathways, dysregulated in cell cycle control and often overexpress MYC and ERBB2 (Supplementary Table 4). HAPTRIG confirms these disruptions in KEGG pathways and in MSigDB (Molecular Signature Database) Hallmark pathways. Interestingly, GSEA<sup>13</sup> of copy-number data also highly ranks these pathways and autophagy, albeit at a lower rank than HAPTRIG. This is likely because GSEA does not incorporate interaction or haploinsufficiency data, resulting in an altered spectrum of prioritized genes relative to HAPTRIG. A second significant

reason that autophagy has not received further exposure in the context of OV is that very few pathway sets include autophagy. In the many thousands of pathways annotated in MSigDB<sup>38</sup>, autophagy is only included in KEGG and GO pathways, as assayed here. Many genes remain to be annotated within pathways<sup>39</sup>, and improved pathway curation will certainly advance pathway analysis tools such as HAPTRIG.

Although loss-of-heterozygosity accompanied by mutations is a recognized phenomenon in breast, ovary, and other cancer, 99.8% of gene deletions in OV show no mutation in the opposing allele. For autophagy genes, mutations in the remaining allele for tumours with heterozygous deletion were not observed. Rather, cumulative gene expression changes from SCNAs contribute to biological phenotypes<sup>40–42</sup>. Reduced gene expression is observed much more commonly than no change in controlled heterozygous deletions<sup>21</sup>, and mRNA correlates with protein expression in ~80–90% of OV mRNAs<sup>22</sup>. Losses of proteostasis genes are likely oncogenic; multiple studies implicate *BECN1* as a haploinsufficient tumour suppressor in mice<sup>17,18</sup>, possibly related to roles in chromosomal segregation during cell division<sup>43,44</sup>. Chromosome instability in human cancers such as OV and BRCA may be further exacerbated by loss of *BRCA1*, a functionally independent tumour suppressor neighbouring *BECN1* (ref. 45) on cytoband 17q21. Early losses in autophagy genes may contribute to the extreme SCNA heterogeneity of OV, but as we have shown here, also provide opportunity for network-targeted therapy.

The prevalence of such monoallelic changes has been largely unappreciated. In all cancer types, more genes are affected by single gene-dose changes than by biallelic deletions, doubling or more amplifications, and mutations combined. Tumour selection for specific chromosomal arm losses or duplications follow enrichments for tumour suppressors or oncogenes, respectively<sup>4,41</sup>. However, methods to interpret effects and implement action on SCNAs have been underdeveloped. Monoallelic SCNAs may sometimes be viewed as a gene-dose equivalent of a passenger mutation, but scoring collaborative and cumulative pathway interactions and alterations and comparing to a permuted control enabled HAPTRIG to sort through this ‘passenger’ noise and yield significant results. We developed the HAPTRIG tool to accurately predict targetable individual gene losses for the autophagy pathway in OV, and have further provided quantitative predictions for all disrupted OV pathways (Supplementary Data 1–4). In addition, we have provided a free web-tool ([https://delaney.shinyapps.io/HAPTRIG\\_Single\\_Module\\_Beta/](https://delaney.shinyapps.io/HAPTRIG_Single_Module_Beta/)) to allow the community to easily perform a HAPTRIG analysis on 21 cancer types with 187 unique KEGG pathways.

We suggest that a roadmap of targetable genetic changes in tumours need not be limited to mutations, and HAPTRIG may therefore reveal additional targetable pathways across cancer types. COAST therapy should be clinically tested in OV, given its strong effects, minimal toxicity<sup>24</sup>, and genetic rationale.

## Methods

**HAPTRIG analysis construction.** HAPTRIG proteostasis networks were built from the KEGG pathways autophagy (hsa04140), Lysosome (hsa04142), endoplasmic reticulum processing (hsa04141), ubiquitin-mediated proteolysis (hsa04120), peroxisome (hsa04146) and the p53 (hsa04115) pathway. The KEGG autophagy pathway was further curated using current knowledge by adding *MAP1LC3B*, encoding the protein most commonly used to define autophagosomes<sup>25</sup>. We used protein–protein interactions (PPIs) from the BioGRID curated database<sup>14</sup> to connect input pathway genes. For the pan-pathway analysis and in quality control networks, all human KEGG pathways were used. The full list of 187 KEGG pathways tested is included in Supplementary Data 1.

We obtained copy-number data ( $N = 579$  tumours for OV) from the UCSC cancer genome Browser<sup>46</sup>, using copy-number calls from the GISTIC2.0 algorithm<sup>47</sup>. For the 2009 OV data sets<sup>16</sup>,  $\log_2$  segmented copy-number data were

used, since the array used was not a SNP6 array. There were 102 serous tumours and 11 endometrioid tumours.

To incorporate information regarding dose sensitivity of genes into our network scores, orthologous data sets were used. Yeast data were extracted (17 August 2015) from YeastMine<sup>48</sup>, with the query ‘Phenotype = Haploinsufficient’ or ‘Phenotype = Haploproficient’. Similar annotations for 169 murine genes were extracted (9/17/2015) from the Mouse Genome Informatics database or the MouseMine database<sup>49</sup>. Human homologues for mouse and yeast genes were systematically determined using the ‘Homology’ tool of MouseMine and YeastMine. Of the 486 proteostasis genes studied, 284 were annotated as gene-dose-sensitive. All gene annotations can be found in Supplementary Table 3.

Each edge connecting two gene nodes was scored for negative (loss or deletion) or positive (gain or amplification) copy-number change as follows. Given an edge between gene1 (G1) and gene2 (G2), edge scores were calculated as:

For either (G1,G2) GISTIC < 0 (at least one gene is deleted):

$$\text{EdgeLossScore}(G1, G2) = \text{Minimum}(\text{GISTIC1} \times \text{GDS1}, \text{GISTIC2} \times \text{GDS2}) \quad (1)$$

For both (G1,G2) GISTIC  $\geq 0$  (neither gene is deleted):

$$\text{EdgeGainScore}(G1, G2) = \text{Maximum}(\text{GISTIC1} \times \text{GDS1}, \text{GISTIC2} \times \text{GDS2}) \quad (2)$$

Wherein GISTIC scores represent a range of (–2, –1, 0, 1, 2) from –2 as a double deletion, –1 as a monoallelic deletion, 0 as no somatic change, 1 as a monoallelic gain and 2 as a gain of two or more alleles, and gene dose sensitivity (GDS) indicates the gene-dose sensitivity information (1 for no information, 2 for yeast information and 3 for mouse information).

For Fig. 2, the pan-pathway analysis utilized only gene edges within the given pathway (for example, only genes within the autophagy pathway). For Fig. 3, wherein interactions between proteostasis pathways were important to consider, edges were also utilized in the analysis if one gene in the edge contained a gene in another proteostasis pathway.

For each pathway within a cancer type, we first calculated for each patient the sum of edge scores. We then normalized to the minimum possible haploinsufficient score of that module (a score in which every gene within the module had a monoallelic loss). We further average these normalized scores across all tumours within a TCGA cohort to produce the colourized depiction of average network score suppression (blue) or enhancement (red) in Fig. 3a.

Each cancer type has a unique distribution of chromosome losses and gains. Since a highly copy-number variable cancer may have a higher chance of a random loss or gain of a pathway than a relatively SCNA stable cancer, we compared the distribution of observed HAPTRIG module scores to that of the distribution of HAPTRIG module scores resulting from globally shuffled gene copy-number data from the same cancer cohort (Supplementary Software 1). Edge scores were then recreated using the shuffled gene data. Two distributions for each cancer type were thus created using identical calculations: an observed HAPTRIG module score distribution corresponding to observed tumour data, and a statistical comparison HAPTRIG module score distribution corresponding to randomized data. To increase the confidence in the output  $P$  value, our automated HAPTRIG code creates 1,000 control network scores for each tumour and output  $P$  values are generated from the average  $\log_{10}(P)$  value resulting from these 1,000 control network comparisons. HAPTRIG score distributions were compared by Student’s  $t$ -test and multiple hypothesis testing corrected by the Bonferroni method (for 6 pathways and 21 cancer types = 126 comparisons in Fig. 3, 187 comparisons—all KEGG pathways—for Fig. 2) to generate a  $q$  value.

Visual networks were drawn using Cytoscape 3.3 (ref. 50). To produce a representative network for the entire OV cohort, the EdgeScores were recomputed at the cohort level using mean GISTIC scores across all tumours. If a node had an SCNA alteration in > 33% of patients, an edge was drawn to its PPI partner (blue: loss, red: gain, purple: antagonistic). To accommodate lower numbers of mutations relative to SCNA events, if a gene reached a mutation rate of above 10%, PPI edges were represented as disrupted by mutations (green edge visualization). Node size and colour represent their frequency of SCNAs: blue for more common losses, red if for more common gains, and green if mutated in > 10% of patients. Node shade represents the prevalence of the most frequent SCNA event. Node outlines are coloured bright cyan if mouse GDS information was incorporated, and light cyan if yeast GDS information was incorporated. Grey edges depict associations of genes with their respective KEGG molecular pathways.

For gene-impact prioritization, EdgeScores were summed among all tumours within a cohort. Scores were then summed for each gene within the proteostasis network (the gene could be on either end of the edge). The sum of scores was used to rank those genes which had the lowest values (genes of highest network score impact for losses) as well as rank those genes that had the highest values (genes of highest network score impact for gains). A summary of the highest and lowest scoring five genes for each KEGG molecular pathway is provided in Supplementary Data 1.

For quality control, a table of the top 10 ranked genes (as in the gene-impact prioritization) for each of the 187 KEGG pathways was generated and compared with the appropriate COSMIC tumour suppressor/oncogene gene set or STOP/GO

gene set. Efficiency was calculated as the per cent of possible hits that were found to be present in the quality control table.

**Code availability.** Complete HAPTRIG code is available as Supplementary Software 1. Demo data for input are provided as a convenience as Supplementary Data 5.

**Gene set enrichment analysis.** TCGA OV data were used as the expression data set, with tumour copy number compared with normal tissue control copy number. Gene sets were the same as HAPTRIG. Gene set permutations were set at 1,000. To find oncogenic pathways, the comparison was TUMOR\_versus\_NORMAL, to find tumour suppressor pathways, the comparison was NORMAL\_versus\_TUMOR. Leading edge analysis was performed and the top 10 genes for each pathway were input as benchmarking genes for quality control analysis, as described above. GSEA version used was 2.2.2.

**Cell culture and reagents.** Established cell lines were purchased from the American Type Culture Collection and validated by short tandem repeat profiling (Promega). Routine microscopic morphology tests were performed before each experiment. Cells were verified to be mycoplasma negative by a PCR assay (Agilent Technologies (Stratagene), cat# 302008). Patient consent was obtained for scientific use and publication of the LPPDOV patient-derived OVs, as previously described<sup>24</sup>. All cells were grown in RPMI (Life Technologies) supplemented with 2% glucose, nonessential amino acids (Mediatech #45000-700), sodium pyruvate (Mediatech #45000-710), antibiotics (penicillin, streptomycin and amphotericin, Mediatech #30-004-CI) and 10% fetal bovine serum (Omega Scientific #FB-11). Cells were cultured at 37 °C with 5% CO<sub>2</sub>.

**Antibodies.** All primary antibodies were used at 1:1,000 dilution. LC3B (Novus Biologicals #NB100-2220), p62 (BD Biosciences #610382),  $\beta$ -actin (Sigma-Aldrich #A5441-2ML), GRP78 (BioLegend #644402), BECN1 (SantaCruz sc-11427), PIK3C3 (Abgent AP1851b), GABARAPL2 (Abgent AP1822d), ATG5 (Cell Signaling 8540P),  $\gamma$ -tubulin (Sigma-Aldrich T6557), GAPDH (GeneTex #239) and DyLight secondary (1:15,000 dilution) antibodies were used: 800 nm for anti-rabbit (VWR #PI35571) and 680 nm for anti-mouse (VWR # PI35518). Secondary horseradish peroxidase antibodies were anti-rabbit (Jackson ImmunoResearch #211-032-171) anti-rat (Life Technologies #619520) or anti-mouse (Jackson ImmunoResearch #115-035-003).

**Drugs.** Docetaxel (Winthrop, US, 20 mg ml<sup>-1</sup> injection concentrate) and cisplatin (Teva Pharmaceuticals, US, 1 mg ml<sup>-1</sup> injectable) were obtained by the Moores Cancer Center pharmacy. Metformin (VWR, cat# 89147-892), rapamycin (LC Labs, cat# R-5000), dasatinib (LC Labs, cat# D-3307) and nelfinavir (Creative Dynamics Inc, special order, or for *in vivo* studies Viracept, Agouron Pharmaceuticals) were purchased in powdered form.

**Knockdown shRNAs.** Knockdowns for *MAP1LC3B* and *BECN1* were purchased from ThermoFisher Scientific (#RHS4533-EG8678). At least two shRNAs were always used to generate the presented figures. PEG400 for *in vivo* drug vehicle was from Spectrum Laboratory Products (#TCI-N0443-500G).

**Transmission electron microscopy.** Three million cells were seeded onto 10 cm tissue culture (TC) plates, grown for 24 h and then treated with control dimethylsulphoxide/water, nelfinavir (10  $\mu$ M), chloroquine (10  $\mu$ M) or COAST (which includes metformin, 10  $\mu$ M, chloroquine, 10  $\mu$ M, nelfinavir, 10  $\mu$ M, rapamycin, 10 nM and dasatinib, 50 nM. Supernatant was removed at 12 h, 10 ml fixative added and incubated at room temperature for 10 min, and then samples were immediately processed by our electron microscopy core. For the analysis, pictures were blinded and then scored using ImageJ to quantify regions of protein aggregates, as measured by high electron density.

**Statistics.** In all figures, \* $P < 0.05$ , \*\* $P < 0.01$ , \*\*\* $P < 0.001$ . *In vivo* tests used Wilcoxon rank-sum with the exception of live subcutaneous tumour measurements, which was tested by analysis of variance two factor with replication (a *t*-test of tumour sizes reaches  $P < 0.05$  at day 2). All other *P* values were calculated using a two-tailed Student's *t*-test unless otherwise noted. All experiments were performed at least three times with combined data quantified and representative images shown, with the exception of mouse and electron microscopy experiments that were performed once. For HAPTRIG tool statistics, refer to HAPTRIG section above.

**In vitro growth inhibition and death assays.** Assay data are from at least four independent experiments. If shRNAs were used, with two or more shRNAs per gene were always tested. A total of 2.5–5k cells were seeded onto 96-well TC-treated plates, allowed to adhere for 30 min and then treated with drugs or control vehicle for a total volume of 100  $\mu$ l. Plates were placed at 37 °C for 48 h unless otherwise indicated. Media was removed and cells were washed once with 125  $\mu$ l PBS. PBS was then removed and 50  $\mu$ l crystal violet stain (0.11% crystal violet, 0.17 M NaCl, 22% MeOH, in water) was added. After 30 min room temperature staining, stain was removed and 125  $\mu$ l PBS was added as a wash. Supernatant was carefully removed to minimize cell disturbance but maximize

removal of unspecific crystal violet. Plates were then dried at 37 °C for 1 h without lids and 85  $\mu$ l MeOH was added to solubilize the crystal violet. Absorbance was read at 600 nm to determine cell density, and background was subtracted. Per cent cell loss was calculated using the formula:  $100 - (100 \times \text{AbsDrug}/\text{AbsControl})$ , which incorporates both slowed growth as well as dead cells.

For specificity calculations in Supplementary Fig. 11, the average growth inhibition of U373 and IGROV1 is subtracted from the average growth inhibition of OVCAR3, 5, 8, 10 and LPPDOV to yield the average per cent difference in growth inhibition between groups, which is termed the Specificity % in the graphs. For Supplementary Fig. 11C, the 17 drug combinations including the labelled drug from Supplementary Fig. 11A were used to obtain a 'Drug Landscape Specificity'. This calculation was: Drug Landscape Specificity =  $\log_2(\text{Survival}(U373)/\text{Survival}(\text{CellLineX}))$ , where survival is the average survival of the 17 drug combinations and CellLineX is one of the OV lines.

For soft agar assays, 0.5% agar/RPMI layer was laid by pipetting 50  $\mu$ l agar into wells of a 96-well plate. The top layer contained 500 cells per 50  $\mu$ l, in 0.3% agar/RPMI. After agar solidified, drugs were added with another 50  $\mu$ l of agar-free RPMI. After 7 days of growth, colonies were stained by 0.005% crystal violet, imaged and analysed for size by ImageJ. To determine number of cells per colony, a duplicate plate was stained immediately after seeding to provide images of single cells. Colony sizes were assumed to be spherical to calculate the number of constituent cells.

For suspension assays, cells were seeded to 100k cells per 4 ml RPMI with or without drug and grown in six-well polyHEMA plates. After 3 days of growth, cells were spun down (500 g, 5 min), washed in PBS, trypsinized 5 min, spun down and washed in PBS again, and then stained by trypan blue to obtain viable single-cell counts via a Vi-Cell XR automated cell counter (Beckman Coulter).

**Autophagic flux microscopy.** OVCAR3 cells with mCherry-GFP-LC3B virally integrated were seeded on a glass bottom 12-well plate to 5,000 cells per well and treated with COAST drugs (chloroquine (10  $\mu$ M, C), nelfinavir (10  $\mu$ M, N), rapamycin (R, 10 nM) and dasatinib (D, 50 nM)). Cells were then imaged live by a Olympus XI-51 spinning disc microscope fitted with an environmental chamber set to standard 5% CO<sub>2</sub> 37 °C conditions.

**Western blotting.** Cells were grown to 50% confluency on 10 cm plates and treated with drugs or control for 24 h at 37 °C. Media was collected, cells washed in PBS and the supernatant was spun 500 g. Iced RIPA buffer (supplemented with a protease inhibitor cocktail (Sigma-Aldrich), 2 mM sodium orthovanadate and 50 mM NaF) was added to solubilize the cells (15 min, room temperature) at which point cells were collected using a cell lifter (Fisher Scientific). Supernatants were added to the RIPA buffer and combined with adherent cell fraction. Lysates were spun at 10,000g for 10 min at 4 °C, and supernatant was saved and quantified by bicinchoninic acid (BCA) assay (Pierce #23235). A measure of 30  $\mu$ g of protein was loaded per well of a 15% SDS-polyacrylamide gel electrophoresis gel and transferred onto polyvinylidene difluoride membrane. The membrane was blocked in 5% dry milk (Genesee Scientific, #20-241) or 0.1% casein (Sigma C5890-500G). Primary antibodies were used at 1:1,000 dilution, and secondary horseradish peroxidase antibodies were used at 1:5,000 dilution or secondary fluorescent antibodies were used at 1:15,000. Fluorescent secondary antibodies were visualized using a LI-COR Odyssey scanner. Quantification of band intensity was performed in ImageJ and all normalizations were to the shown loading control. For uncropped western blots, refer to Supplementary Fig. 17.

**Flow cytometry.** Flow cytometry was performed on a BD FACS Calibur cytometer and analysed with BD CellQuest Pro.

**Propidium iodide viability staining.** A total of 100,000 cells were grown in a six-well TC dish with 3 ml media containing drug or control solution for 48 h. Media was collected, cells were washed with 1 ml PBS, which was pooled with the media, and then cells were trypsinized for 5 min in 1 ml Trypsin-EDTA. Trypsinized cells were then combined with supernatants, cells were centrifuged for 5 min at 500g and then resuspended in 400  $\mu$ l iced PBS containing 1  $\mu$ g ml<sup>-1</sup> propidium iodide. Cells were then analysed on the flow cytometer.

**Acridine orange autophagosome staining.** A total of 100,000 cells were grown in a six-well TC dish with 3 ml media containing drug or control solution for indicated time points, staggered from the latest time point. Media was removed and adherent cells were stained by 1  $\mu$ g ml<sup>-1</sup> acridine orange for 15 min. Staining solution was aspirated, cells were washed once in 1 ml PBS, and then cells were trypsinized for 5 min in 1 ml Trypsin-EDTA. Trypsinized cells were then combined with 1 ml iced RPMI and centrifuged for 5 min at 500g. Supernatant was aspirated and cells were resuspended in 400  $\mu$ l iced PBS. Cells were then analysed on the flow cytometer.

**Mouse models.** All animal protocols were approved by the Institutional Animal Care and Use Committee (IACUC) of University of California: San Diego (UCSD), and all rules and regulations were followed during experimentation on animals. Experiments were powered to detect differences of 30% (<http://homepage.divms.uiowa.edu/~rlenth/Power/>). No blinding was performed, since drug and control solutions were visually distinguishable. All mice were

female, and COAST doses (250 mg kg<sup>-1</sup> nelfinavir, 30 g kg<sup>-1</sup> chloroquine, 2.24 mg kg<sup>-1</sup> rapamycin, 150 mg kg<sup>-1</sup> metformin and 4 mg kg<sup>-1</sup> dasatinib, daily by gavage in 50% PEG400 in water) were determined using clinically safe doses as determined from a previous study<sup>24</sup>. All mice were included for the following experiments if above 18 g starting weight and with a healthy disposition before any injections. No mice were censored in these experiments.

In the subcutaneous model, 5 × 10<sup>6</sup> OVCAR3 cells were injected into the right flank of 8–10-week-old female nude Nu/nu mice (N = 7 per group). Mice were randomized when tumours were palpable. Treatment with control (gavage, daily, 50% PEG400) or COAST began when tumours reached 100 mm<sup>3</sup>, which was 14–20 days after cell injection. Mice were treated for 7 days and then killed 3 h following the last treatment. Tumours were removed and weighed as additional confirmation of the caliper size measurements.

For the chemo-resistant model, 5 × 10<sup>6</sup> early passage LPPDOV cells were injected intraperitoneal (i.p.) into a female Nu/nu mouse, allowed to develop visible tumours, and ascites were collected and plated in complete RPMI on a TC-treated Petri dish. Non-adherent blood cells were washed off with RPMI, and then the adherent cells were trypsinized and transferred to a non-TC-treated plate for amplification. As soon as sufficient cells were grown to inject a cohort of mice (<5 passages), 3 million cells were injected i.p. into 8–10-week-old female Nu/nu mice. After injection, groups were normalized and randomized for mouse weight (N = 10 for control group, N = 7 for chemotherapy group and N = 9 for COAST group). Ten days post cell injection, daily gavaging of COAST or control (50% PEG400) was performed for 15 days. In the cisplatin/docetaxel group, mice were additionally injected i.p. with 1 mg kg<sup>-1</sup> cisplatin and 2.5 mg kg<sup>-1</sup> docetaxel once per week starting at the first control treatment day for 2 weeks.

For the syngeneic OV model, 3 × 10<sup>6</sup> mCherry labelled ID8-IP cells<sup>27</sup>, which have been passaged in the peritoneal cavity, were injected i.p. into syngeneic female C57BL/6 mice at 10 weeks of age. Mice of equal mean weights were used in each group (N = 8 per group), randomized post-injection, and are the same cohort summarized in a previous study of ours<sup>24</sup>. Fourteen days after injection, one group received daily (seven times a week) vehicle gavage injections (50% PEG400), the C + N group received daily chloroquine and nelfinavir gavage (30 and 250 mg kg<sup>-1</sup>, respectively) and the COAST group received daily COAST gavage. Mice were monitored daily for distended abdomens following the first treatment injections. All mice were killed when ascites formation produced visible discomfort to control animals, which occurred after 14 days of treatment (28 days since cell injection). The peritoneum of the mice was exposed and any visible nodules on the peritoneum wall were surgically dissected along with the liver and ovaries. These tissues were then imaged with the OV100 Small Animal Imaging System (Olympus). Bright-field, GFP and mCherry channel information were collected and only red fluorescent (but not green autofluorescent) punctae area was quantified in ImageJ. Fluorescent area was mathematically converted into tumour volume assuming spherical shape of the tumour and circular shape of the fluorescent area. Any bloody ascites present upon initial opening of the peritoneum was transferred by P1000 micropipette into a 15 ml conical tube and volume determined by micropipette. In the longer-term safety experiment, the experiment was performed identically, except mice were treated by COAST for a period of 8 weeks with five daily doses (daily excluding weekends).

**Data availability.** All the data that support the findings of this study are available within the article and Supplementary Files, or available from the authors upon request.

## References

- McLeod, H. L. Cancer pharmacogenomics: early promise, but concerted effort needed. *Science* **339**, 1563–1566 (2013).
- McCarthy, J. J., McLeod, H. L. & Ginsburg, G. S. Genomic medicine: a decade of successes, challenges, and opportunities. *Sci. Transl. Med.* **5**, 189sr184 (2013).
- Le, D. T. *et al.* PD-1 blockade in tumours with mismatch-repair deficiency. *N. Engl. J. Med.* **372**, 2509–2520 (2015).
- Davoli, T. *et al.* Cumulative haploinsufficiency and triplosensitivity drive aneuploidy patterns and shape the cancer genome. *Cell* **155**, 948–962 (2013).
- Zack, T. I. *et al.* Pan-cancer patterns of somatic copy number alteration. *Nat. Genet.* **45**, 1134–1140 (2013).
- Ciriello, G. *et al.* Emerging landscape of oncogenic signatures across human cancers. *Nat. Genet.* **45**, 1127–1133 (2013).
- Deutschbauer, A. M. *et al.* Mechanisms of haploinsufficiency revealed by genome-wide profiling in yeast. *Genetics* **169**, 1915–1925 (2005).
- Kandoth, C. *et al.* Mutational landscape and significance across 12 major cancer types. *Nature* **502**, 333–339 (2013).
- Martincorena, I. *et al.* Tumour evolution. High burden and pervasive positive selection of somatic mutations in normal human skin. *Science* **348**, 880–886 (2015).
- Kamihara, J., Rana, H. Q. & Garber, J. E. Germline TP53 mutations and the changing landscape of Li-Fraumeni syndrome. *Hum. Mutat.* **35**, 654–662 (2014).
- Humphrey, S. J., James, D. E. & Mann, M. Protein phosphorylation: a major switch mechanism for metabolic regulation. *Trends Endocrinol. Metab.* **26**, 676–687 (2015).
- Boone, C., Bussey, H. & Andrews, B. J. Exploring genetic interactions and networks with yeast. *Nat. Rev. Genet.* **8**, 437–449 (2007).
- Subramanian, A. *et al.* Gene set enrichment analysis: a knowledge-based approach for interpreting genome-wide expression profiles. *Proc. Natl Acad. Sci. USA* **102**, 15545–15550 (2005).
- Chatr-Aryamontri, A. *et al.* The BioGRID interaction database: 2015 update. *Nucleic Acids Res.* **43**, D470–D478 (2015).
- Forbes, S. A. *et al.* COSMIC: exploring the world's knowledge of somatic mutations in human cancer. *Nucleic Acids Res.* **43**, D805–D811 (2015).
- Etemadmoghadam, D. *et al.* Integrated genome-wide DNA copy number and expression analysis identifies distinct mechanisms of primary chemoresistance in ovarian carcinomas. *Clin. Cancer Res.* **15**, 1417–1427 (2009).
- Qu, X. *et al.* Promotion of tumorigenesis by heterozygous disruption of the beclin 1 autophagy gene. *J. Clin. Invest.* **112**, 1809–1820 (2003).
- Yue, Z., Jin, S., Yang, C., Levine, A. J. & Heintz, N. Beclin 1, an autophagy gene essential for early embryonic development, is a haploinsufficient tumor suppressor. *Proc. Natl Acad. Sci. USA* **100**, 15077–15082 (2003).
- Guo, J. Y. & White, E. Autophagy is required for mitochondrial function, lipid metabolism, growth, and fate of KRAS(G12D)-driven lung tumors. *Autophagy* **9**, 1636–1638 (2013).
- Delneri, D. *et al.* Identification and characterization of high-flux-control genes of yeast through competition analyses in continuous cultures. *Nat. Genet.* **40**, 113–117 (2008).
- Cai, Y. *et al.* Loss of chromosome 8p governs tumor progression and drug response by altering lipid metabolism. *Cancer Cell* **29**, 751–766 (2016).
- Zhang, H. *et al.* Integrated proteogenomic characterization of human high-grade serous ovarian cancer. *Cell* **166**, 755–765 (2016).
- Klionsky, D. J. *et al.* Guidelines for the use and interpretation of assays for monitoring autophagy (3rd edition). *Autophagy* **12**, 1–222 (2016).
- Delaney, J. R. *et al.* A strategy to combine pathway-targeted low toxicity drugs in ovarian cancer. *Oncotarget* **6**, 31104–31118 (2015).
- Klionsky, D. J. *et al.* Guidelines for the use and interpretation of assays for monitoring autophagy. *Autophagy* **8**, 445–544 (2012).
- Bruning, A. *et al.* Nelfinavir induces the unfolded protein response in ovarian cancer cells, resulting in ER vacuolization, cell cycle retardation and apoptosis. *Cancer Biol. Ther.* **8**, 226–232 (2009).
- Ward, K. K. *et al.* Inhibition of focal adhesion kinase (FAK) activity prevents anchorage-independent ovarian carcinoma cell growth and tumor progression. *Clin. Exp. Metastasis* **30**, 579–594 (2013).
- Schwarz, R. F. *et al.* Spatial and temporal heterogeneity in high-grade serous ovarian cancer: a phylogenetic analysis. *PLoS Med.* **12**, e1001789 (2015).
- Fehrmann, R. S. *et al.* Gene expression analysis identifies global gene dosage sensitivity in cancer. *Nat. Genet.* **47**, 115–125 (2015).
- Domcke, S., Sinha, R., Levine, D. A., Sander, C. & Schultz, N. Evaluating cell lines as tumour models by comparison of genomic profiles. *Nat. Commun.* **4**, 2126 (2013).
- Mitra, A. K. *et al.* *In vivo* tumor growth of high-grade serous ovarian cancer cell lines. *Gynecol. Oncol.* **138**, 372–377 (2015).
- Wen, Y. *et al.* Antagonism of tumoral prolactin receptor promotes autophagy-related cell death. *Cell Rep.* **7**, 488–500 (2014).
- Ince, T. A. *et al.* Characterization of twenty-five ovarian tumour cell lines that phenocopy primary tumours. *Nat. Commun.* **6**, 7419 (2015).
- Bowtell, D. D. *et al.* Rethinking ovarian cancer II: reducing mortality from high-grade serous ovarian cancer. *Nat. Rev.* **15**, 668–679 (2015).
- Poole, B. & Ohkuma, S. Effect of weak bases on the intralysosomal pH in mouse peritoneal macrophages. *J. Cell Biol.* **90**, 665–669 (1981).
- Cancer Genome Atlas Research Network. Integrated genomic analyses of ovarian carcinoma. *Nature* **474**, 609–615 (2011).
- Patch, A. M. *et al.* Whole-genome characterization of chemoresistant ovarian cancer. *Nature* **521**, 489–494 (2015).
- Liberzon, A. *et al.* Molecular signatures database (MSigDB) 3.0. *Bioinformatics* **27**, 1739–1740 (2011).
- Hwang, T. H. *et al.* Large-scale integrative network-based analysis identifies common pathways disrupted by copy number alterations across cancers. *BMC Genomics* **14**, 440 (2013).
- Xue, W. *et al.* A cluster of cooperating tumor-suppressor gene candidates in chromosomal deletions. *Proc. Natl Acad. Sci. USA* **109**, 8212–8217 (2012).
- Liu, Y. *et al.* Deletions linked to TP53 loss drive cancer through p53-independent mechanisms. *Nature* **531**, 471–475 (2016).
- Tschaharganeh, D. F., Bosbach, B. & Lowe, S. W. Coordinated tumor suppression by chromosome 8p. *Cancer Cell* **29**, 617–619 (2016).
- Fremont, S. *et al.* Beclin-1 is required for chromosome congression and proper outer kinetochore assembly. *EMBO Rep.* **14**, 364–372 (2013).
- Mathew, R. *et al.* Autophagy suppresses tumor progression by limiting chromosomal instability. *Genes Dev.* **21**, 1367–1381 (2007).
- Laddha, S. V., Ganesan, S., Chan, C. S. & White, E. Mutational landscape of the essential autophagy gene BECN1 in human cancers. *Mol. Cancer Res.* **12**, 485–490 (2014).

46. Goldman, M. *et al.* The UCSC Cancer Genomics Browser: update 2015. *Nucleic Acids Res.* **43**, D812–D817 (2015).
47. Mermel, C. H. *et al.* GISTIC2.0 facilitates sensitive and confident localization of the targets of focal somatic copy-number alteration in human cancers. *Genome Biol.* **12**, R41 (2011).
48. Balakrishnan, R. *et al.* YeastMine--an integrated data warehouse for *Saccharomyces cerevisiae* data as a multipurpose tool-kit. *Database* **2012**, bar062 (2012).
49. Motenko, H., Neuhauser, S. B., O'Keefe, M. & Richardson, J. E. MouseMine: a new data warehouse for MGI. *Mamm. Genome* **26**, 325–330 (2015).
50. Shannon, P. *et al.* Cytoscape: a software environment for integrated models of biomolecular interaction networks. *Genome Res.* **13**, 2498–2504 (2003).

### Acknowledgements

This work was supported by NCI grants CA107263 (D.G.S.), CA102310 (D.D.S.), CA177519 (O.H.) and by funding from the Nine Girls Ask Foundation (D.G.S., D.D.S.). The authors thank Dr. Beth Levine (University of Texas Southwestern) and Dr. Albert La Spada (University of California San Diego) for providing reagents.

### Author contributions

J.R.D. and D.G.S. conceived the experiments and wrote the manuscript. D.D.S., O.H., C.S. and I.T. conceived experiments. J.R.D. built the HAPTRIG tool. J.R.D., S.H. and O.H. performed pilot TCGA data analysis. All other authors and J.R.D. performed experiments.

### Additional information

**Supplementary Information** accompanies this paper at <http://www.nature.com/naturecommunications>

**Competing financial interests:** The authors declare no competing financial interests.

**Reprints and permission** information is available online at <http://npg.nature.com/reprintsandpermissions/>

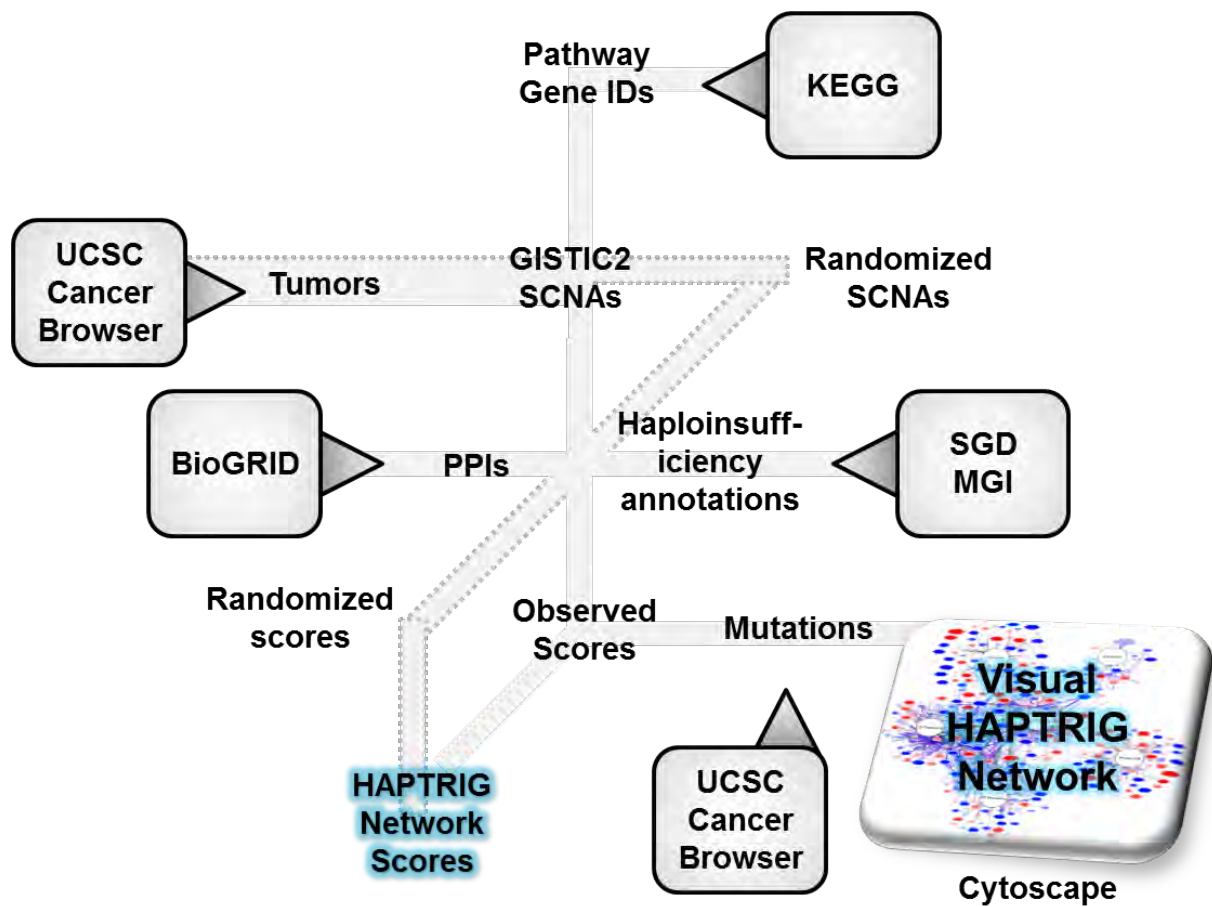
**How to cite this article:** Delaney, J. R. *et al.* Haploinsufficiency networks identify targetable patterns of allelic deficiency in low mutation ovarian cancer. *Nat. Commun.* **8**, 14423 doi: 10.1038/ncomms14423 (2017).

**Publisher's note:** Springer Nature remains neutral with regard to jurisdictional claims in published maps and institutional affiliations.

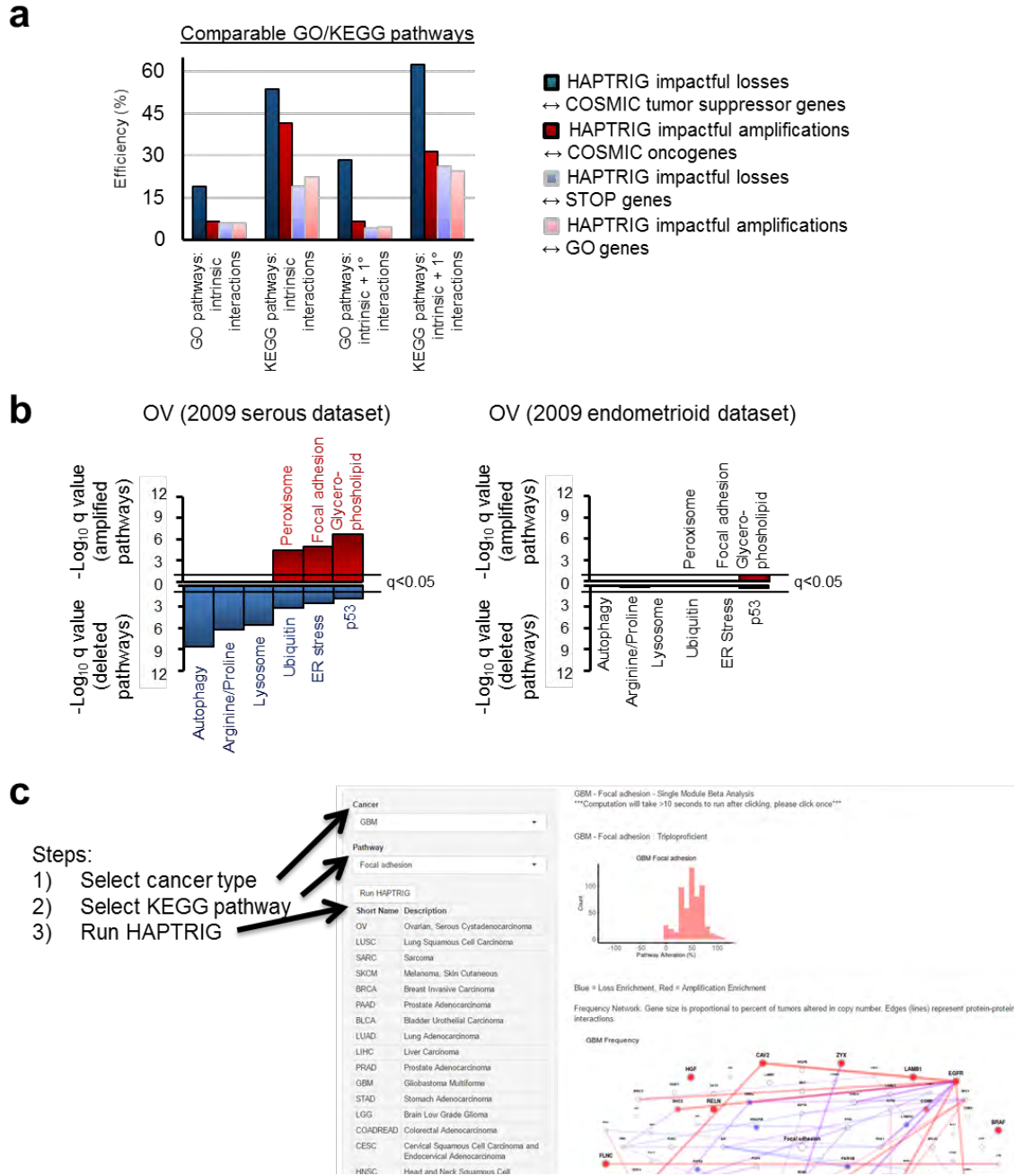


This work is licensed under a Creative Commons Attribution 4.0 International License. The images or other third party material in this article are included in the article's Creative Commons license, unless indicated otherwise in the credit line; if the material is not included under the Creative Commons license, users will need to obtain permission from the license holder to reproduce the material. To view a copy of this license, visit <http://creativecommons.org/licenses/by/4.0/>

© The Author(s) 2017



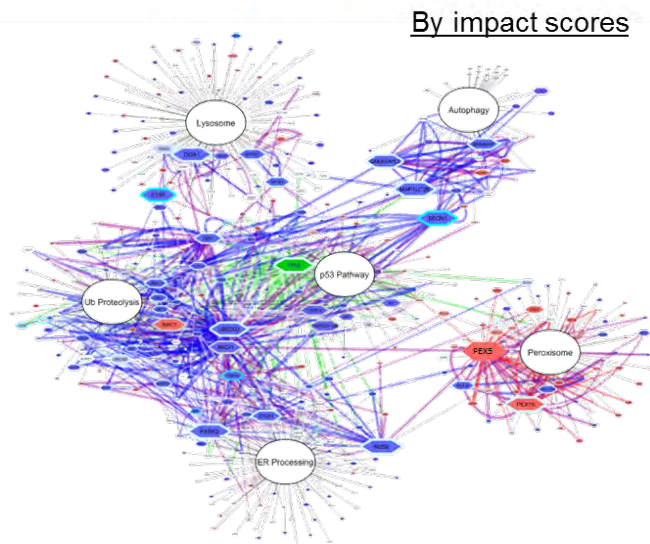
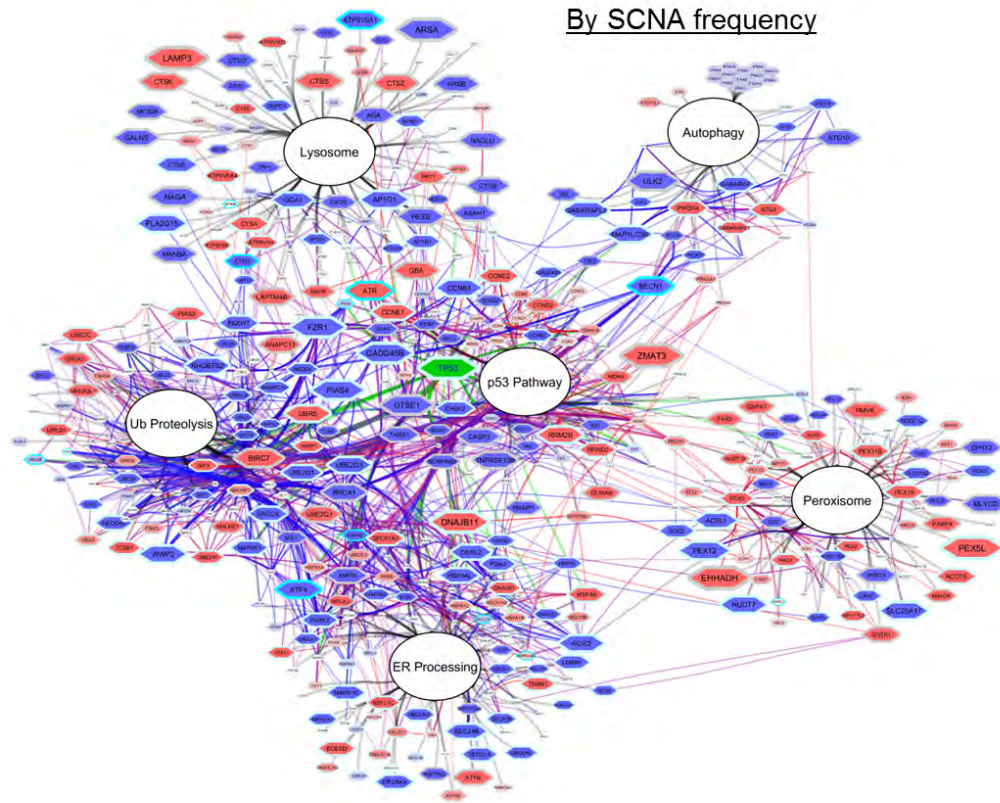
**Supplementary Figure 1. HAPTRIG network scoring workflow.** Data and annotation sources are indicated by filled boxes. Outputs from sources are indicated by overlaid text. Calculations can be found in Methods or Supplemental Software 1.



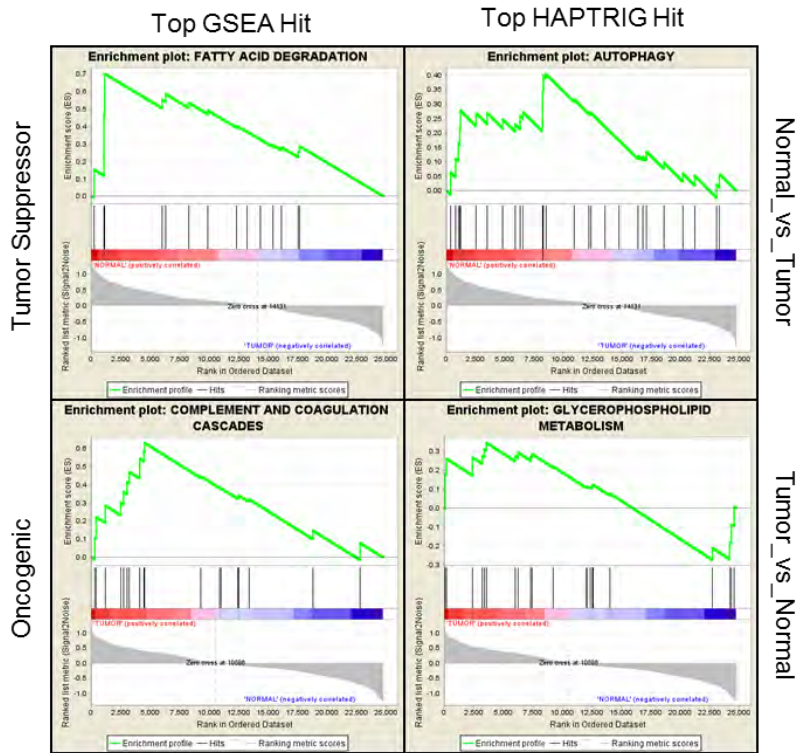
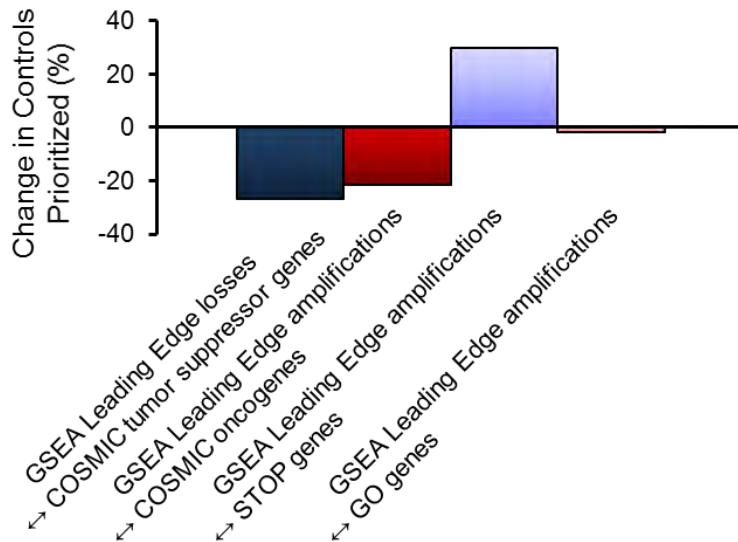
**Supplementary Figure 2. Additional HAPTRIG controls and datasets.** (a) Comparable GO/KEGG pathways (see Supplementary Data 4. Includes proteostasis pathways and 11 other tumor-related pathways) were scored by HAPTRIG, either using only protein-protein interactions within a pathway (intrinsic) or with protein-protein interactions which could include a gene outside the pathway (1° interactions). Unlike the 187-pathway analysis, 1° interactions better prioritized KEGG tumor suppressor genes and thus were used in the proteostasis network scores for Fig. 3. (b) Additional, independent OV datasets were used to verify HAPTRIG findings. As expected, proteostasis pathways were downregulated in the serous dataset, but not the endometrioid dataset. Using all 187 pathways, autophagy was the #2 suppressed pathway in the serous dataset (Supplementary Data 2), but did not reach significance in the endometrioid dataset (Supplementary Data 3). (c) Screenshot from the free, available web tool to perform systematic HAPTRIG analysis on 21 cancer types and 187 KEGG pathways.

The tool is available at:

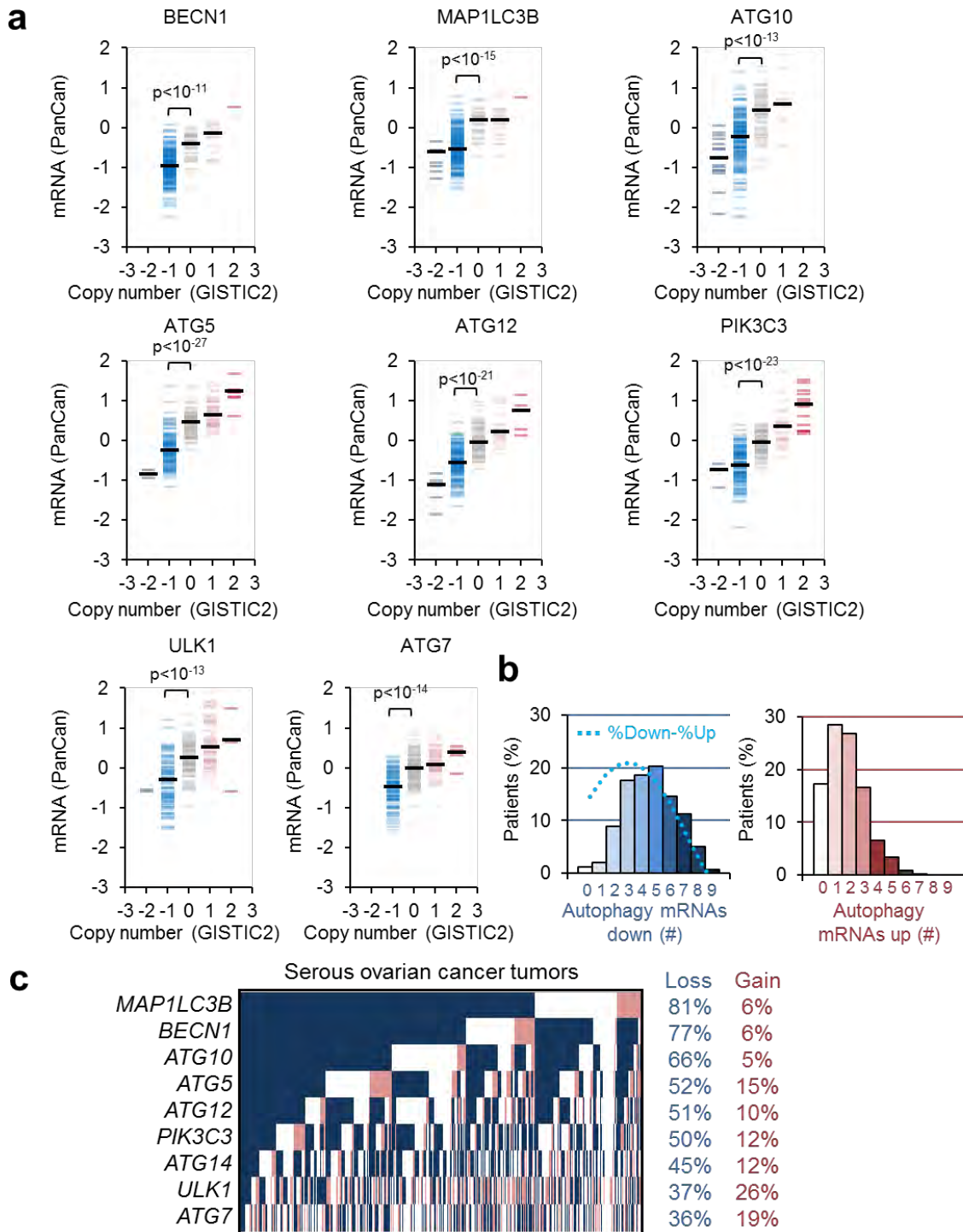
[https://delaney.shinyapps.io/HAPTRIG\\_Single\\_Module\\_Beta/](https://delaney.shinyapps.io/HAPTRIG_Single_Module_Beta/)



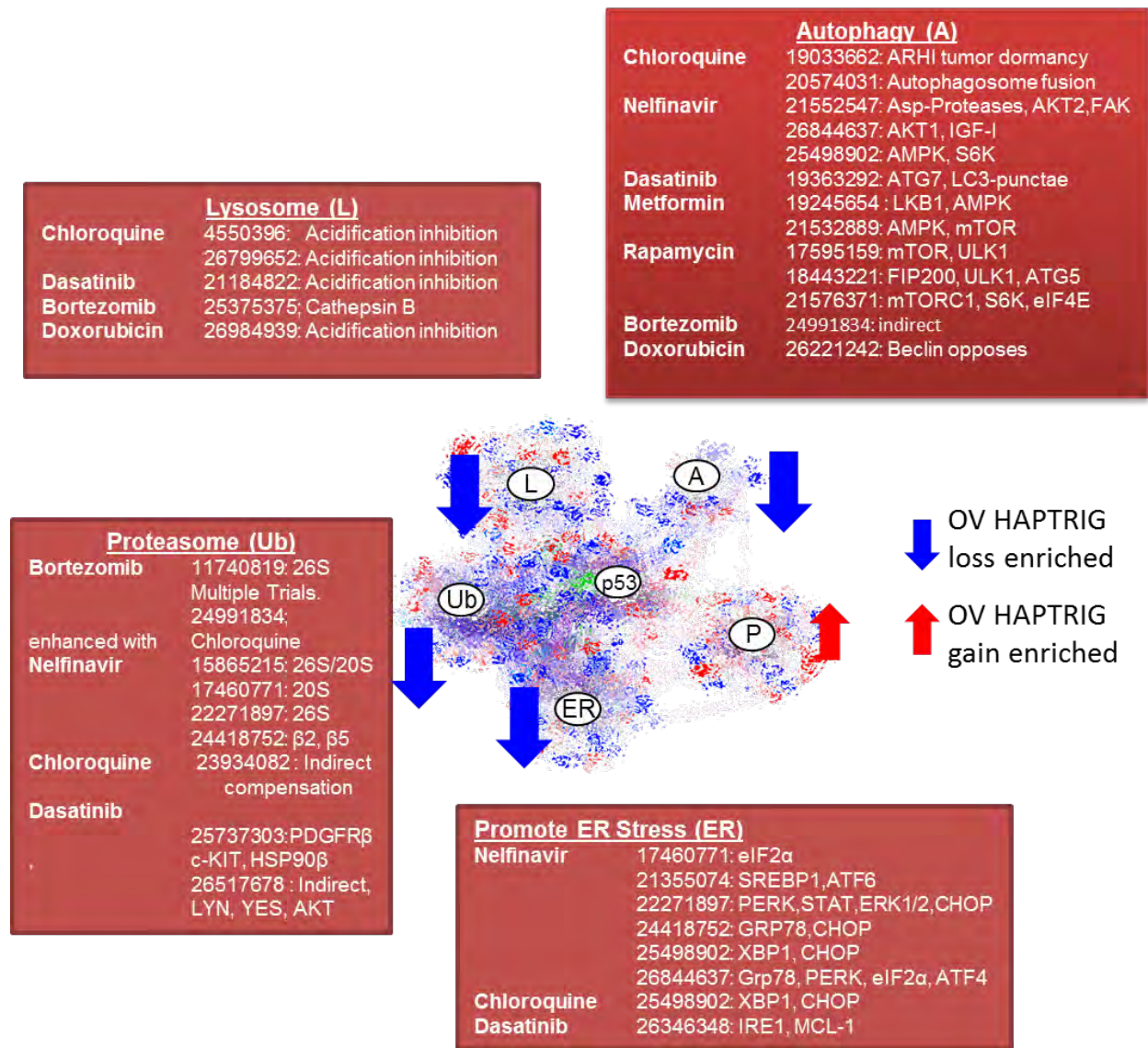
**Supplementary Figure 3. Visual HAPTRIG networks for OV.** Gene nodes and edge protein-protein interactions are displayed with size proportionate to the prevalence of the gene change within the cancer type (top panel) or by the level of the gene's impact on pathways as scored by HAPTRIG (bottom panel). Edges are only drawn if one gene is affected by copy number changes in >33% of patient tumors (top panel) or if the impact of one gene in the edge is 1 z-score away from the mean impact (bottom panel). A red color is assigned if the majority of copy number changes are positive, and blue if they are negative. Green fill and edges indicate genes mutated in >10% of the tumor cohort. Node outlines are highlighted in cyan if haploinsufficiency annotations are associated with that gene: bright cyan if murine evidence exists and light cyan if yeast homologue evidence was found. Grey edges connect genes to corresponding KEGG pathways. *IFNA* genes are visually clustered due to their locally arrayed position on chromosome 9p21.3.

**a****GSEA Plots****b**

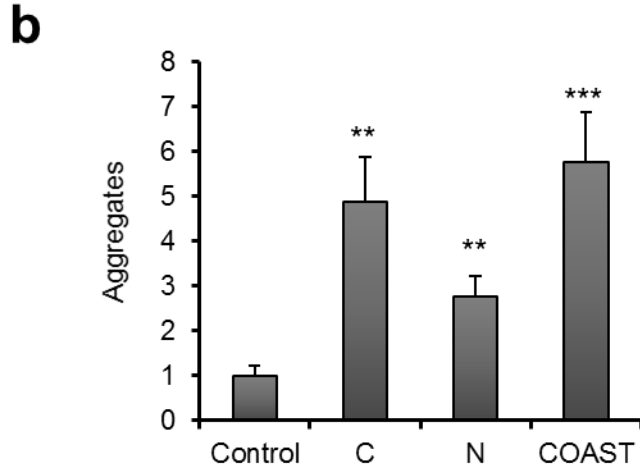
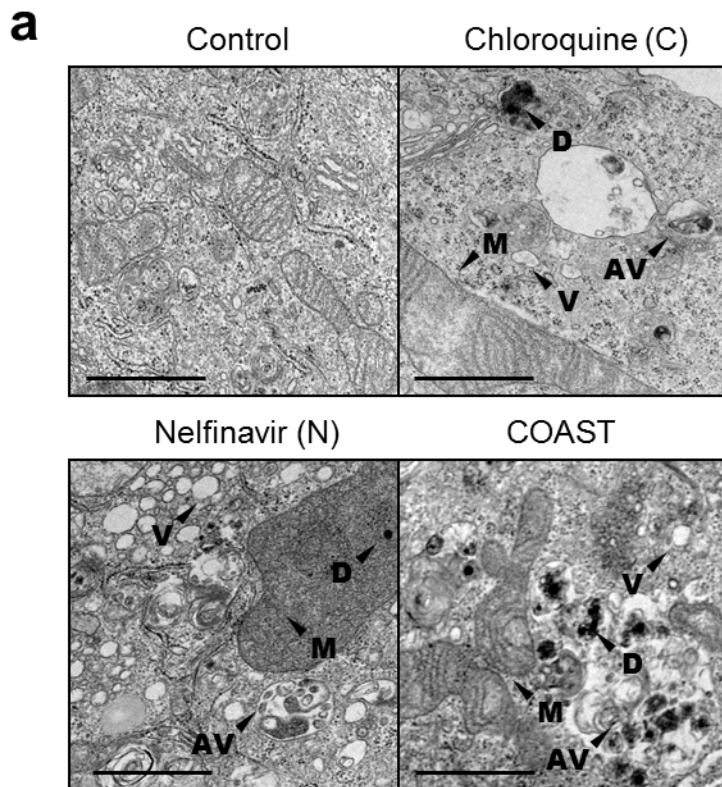
**Supplementary Figure 4. Comparison of HAPTRIG to GSEA.** (a) Copy-number data for OV was input into GSEA using identical pathways as HAPTRIG. Results of GSEA for top-hit tumor suppressors and oncogenic pathways are shown for both GSEA and HAPTRIG. All pathways and direct comparisons are enumerated in Supplemental Data 8. (b) Benchmarking of GSEA in comparison to HAPTRIG was performed as in Figure 1. HAPTRIG identified more tumor suppressor genes and oncogenes as most impactful compared to leading edge analysis of GSEA, but the opposite was observed for prioritization of STOP genes, suggesting the methods are complementary.



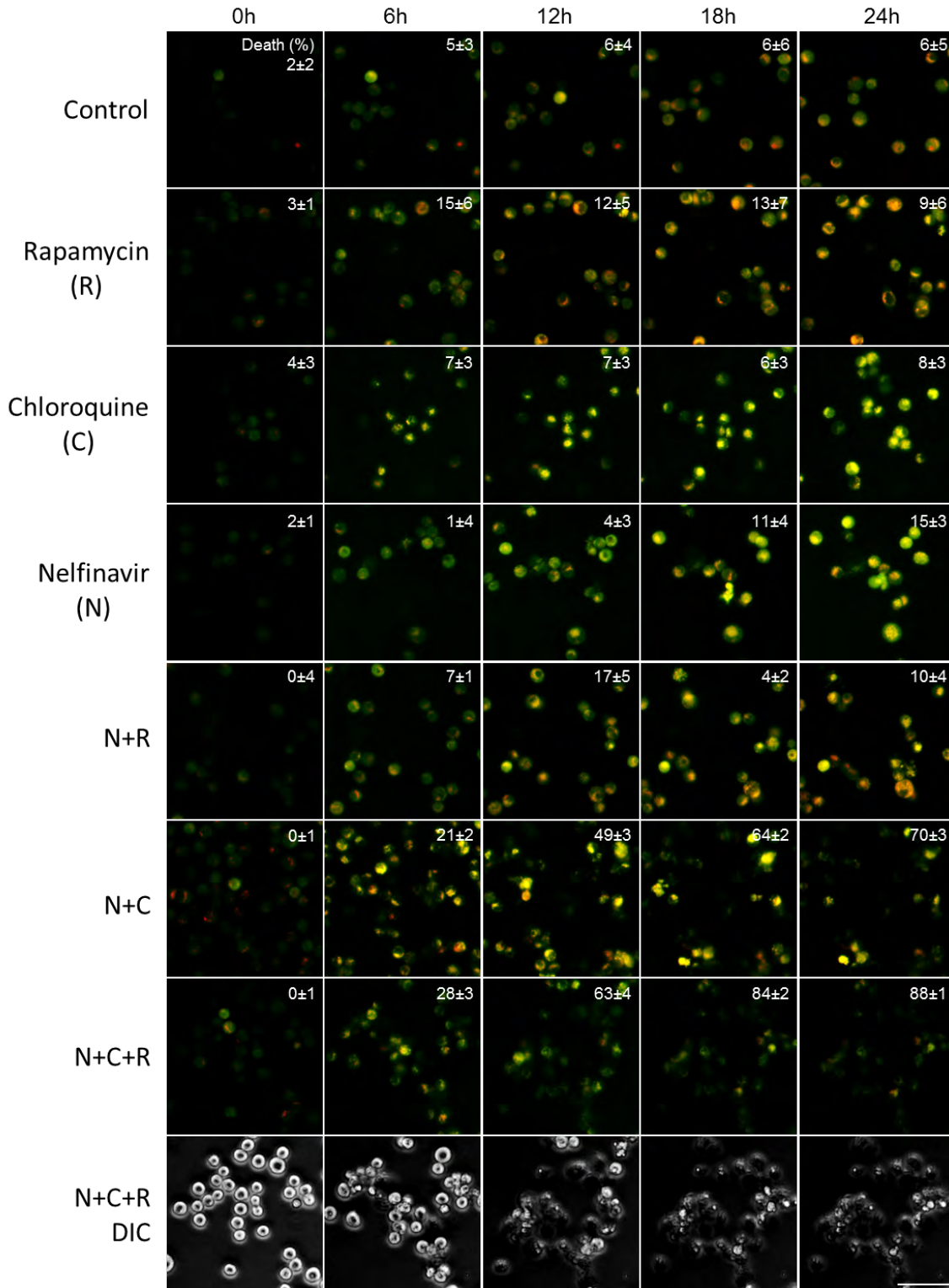
**Supplementary Figure 5. Monoallelic losses of autophagy genes match mRNA suppression.** (a) GISTIC2 calls of core autophagy genes are compared to microarray RNA expression levels within OV. Microarray mRNA comparisons are displayed since there are a higher number of samples than RNAseq. (b) Per patient data on number of autophagy mRNA displaying downregulation versus upregulation. Z score and EXP score cutoffs were set at  $\pm 0.5$ . Autophagy gene queries match the canonical core initiation genes shown in (a). (c) TCGA OV tumors are compared for coincident losses of autophagy genes: each column represents a single tumor. Blue corresponds to allelic deletion, red to allelic gain.

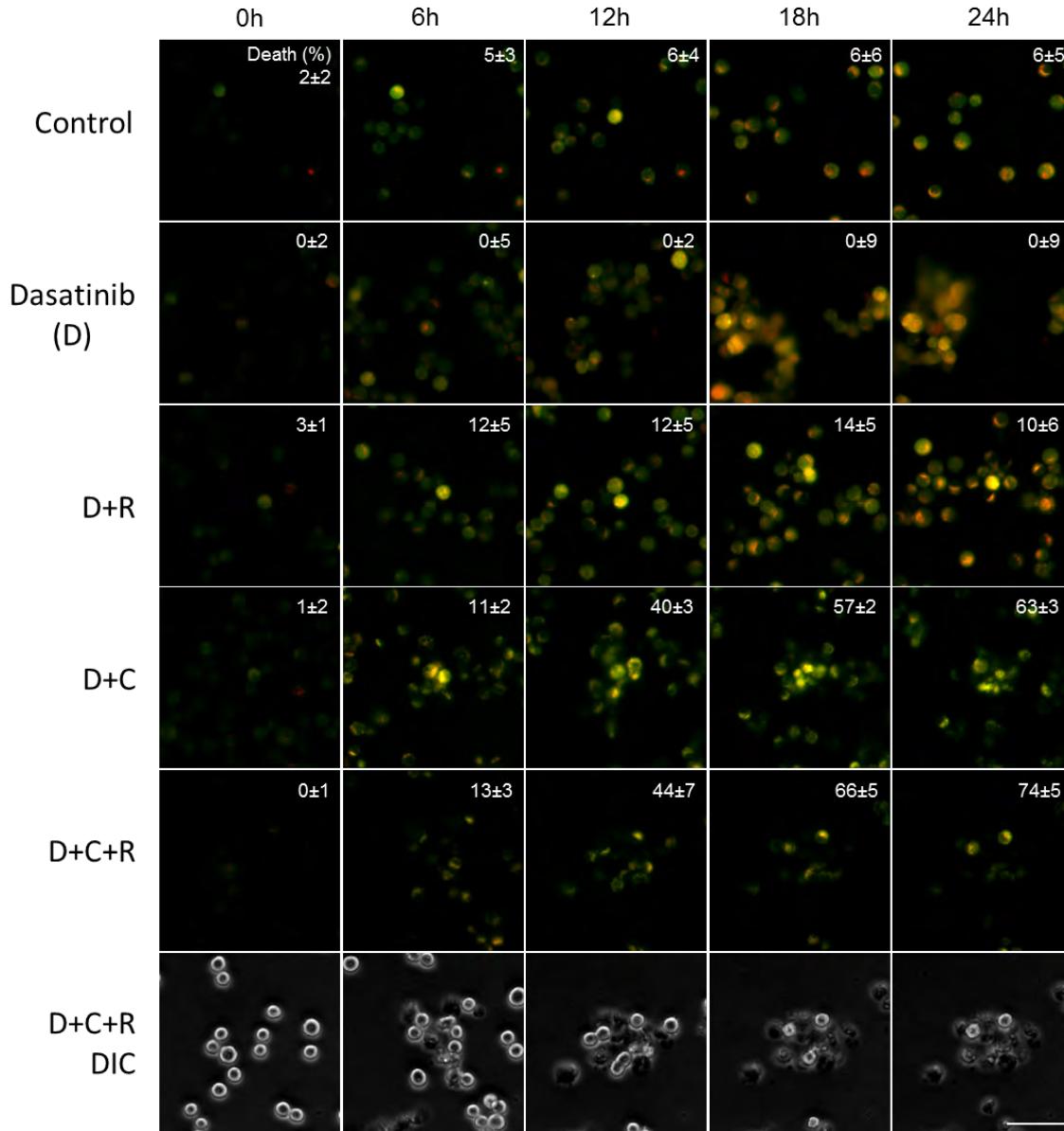


**Supplementary Figure 6. Approved drugs targeting the monoallelically disrupted proteostasis pathways of OV.** Summary of altered proteostasis pathways in OV and FDA-approved drugs impacting the pathway, with corresponding publication report (PMID number shown).

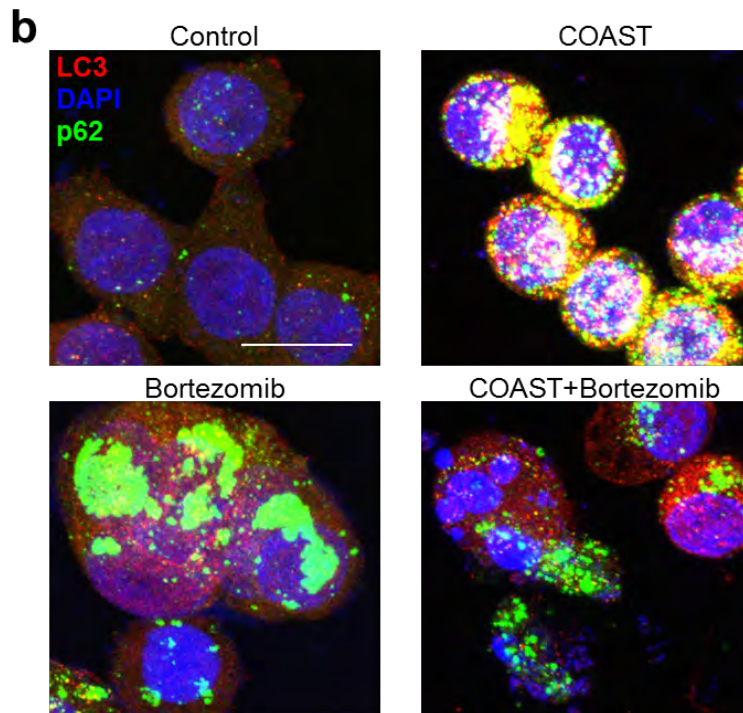
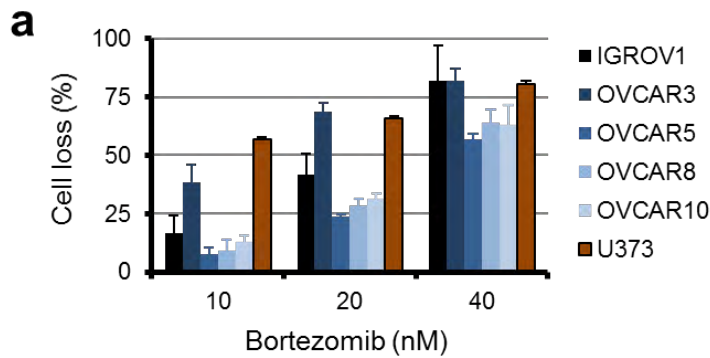


**Supplementary Figure 7. Quantitation of protein aggregation by electron microscopy.** (a) Transmission electron micrographs of OVCAR3 cells treated for 12 hours with COAST components or the full combination (metformin 10 $\mu$ M, chloroquine 10 $\mu$ M, nelfinavir 10 $\mu$ M, rapamycin 10nM, and/or dasatinib, 50nM). Labels: M, Mitochondria, V, Vesicle, AV, Autophagic Vesicle, D, Dense protein aggregate. Scale bar is 1 $\mu$ m. (b) Images were blinded and then quantified for electron dense protein aggregates. Data represent mean  $\pm$  s.e.m. from a single experiment. Aggregate quantitation is relative to control cells. \*\* $p < 0.01$ , \*\*\* $p < 0.001$  by two-tailed student's t-test.





**Supplementary Figure 8. Live autophagic flux microscopy of COAST on OVCAR3 cells.** OVCAR3 cells with a virally integrated mCherry-GFP-LC3 construct were studied for autophagic flux by live microscopy. Autophagolysosome formation quenches the GFP signal due to acidification, which mCherry is resistant to and remains fluorescing red. Yellow punctae thus primarily represent autophagosome structures which have not passed the lysosome fusion stage. Cells were treated with drugs (COAST component drugs which included chloroquine (C, 10 $\mu$ M), nelfinavir (N, 10 $\mu$ M), rapamycin (R, 100nM), and/or dasatinib (D, 100nM)) and then imaged live in normal cell culture conditions by spinning disc microscopy. Lysed cell percentages are shown by inset text. Three independent experiments were performed with representative images shown, numbers represent mean  $\pm$  s.e.m. Scale bar is 40 $\mu$ m.

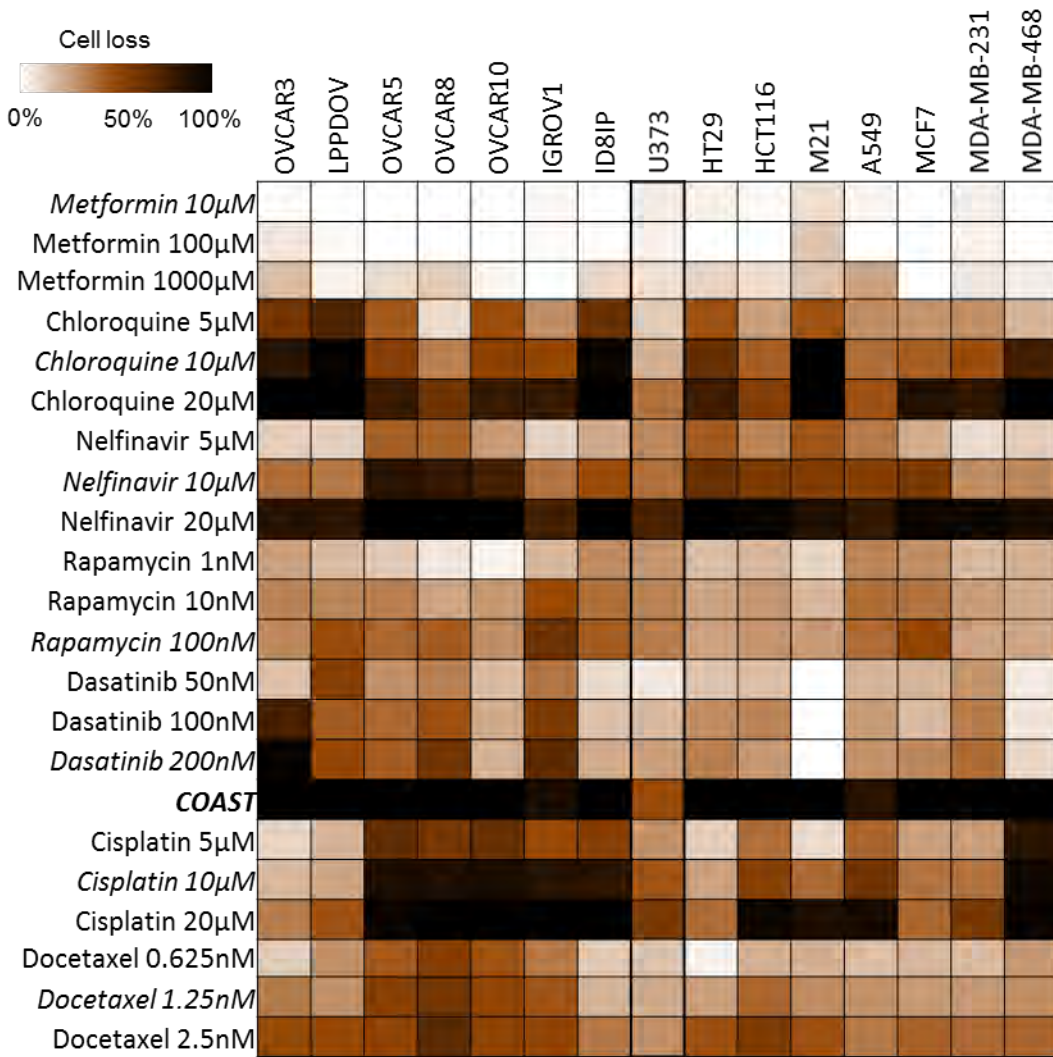


**c**

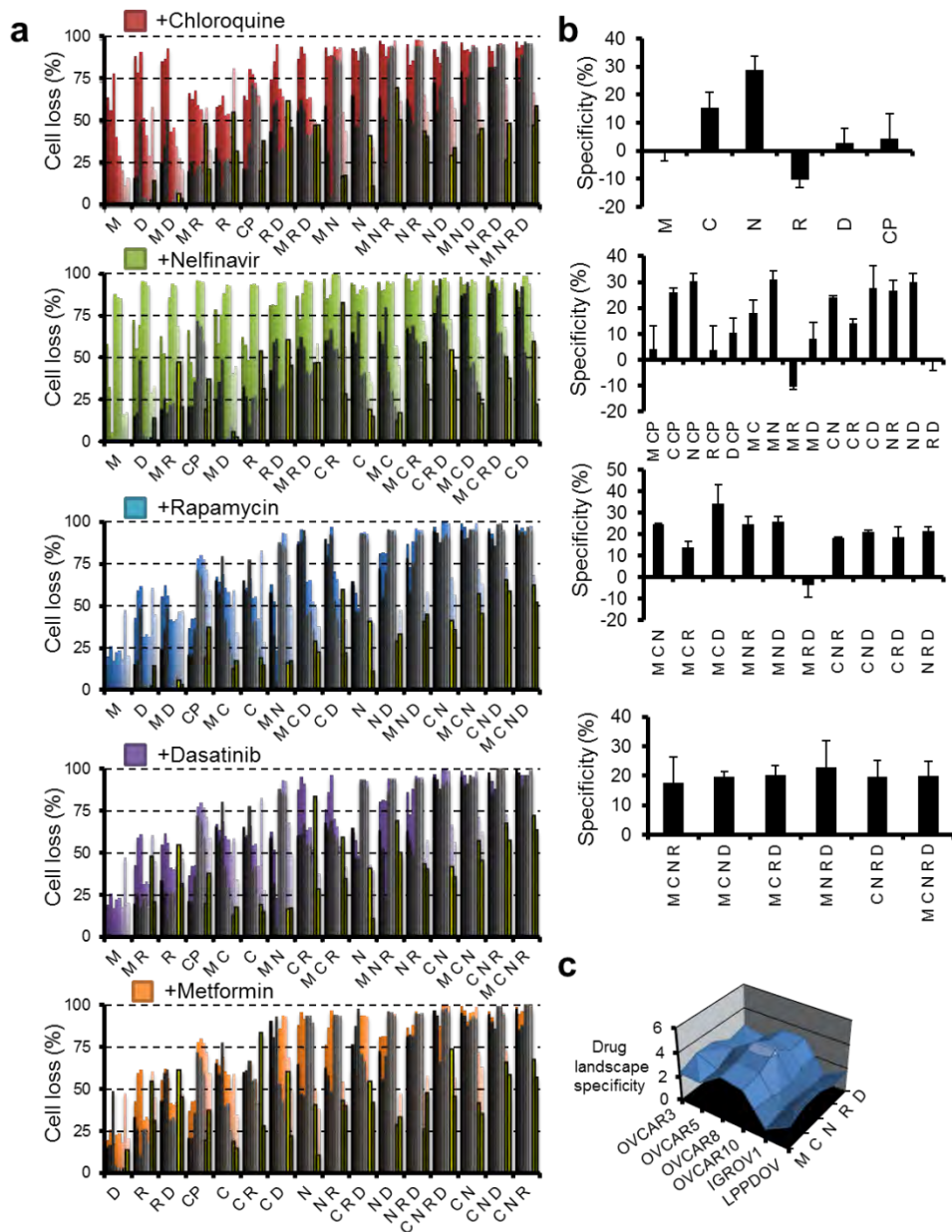
Most frequent adverse event

Drug	G1-2	G3	G4	Safety reference
Chloroquine	2%	-	-	PMID 10759574
Nelfinavir	17%	-	-	FDA (NDA 21-503)
Rapamycin	35%	15%	2%	PMID 21752435
Dasatinib	17%	5%	-	FDA (NDA 21-986)
Metformin	8-13%	-	-	PMID 17638715
<b>Bortezomib</b>	<b>100%</b>	<b>61%</b>	<b>14%</b>	<b>FDA (NDA 21-602)</b>

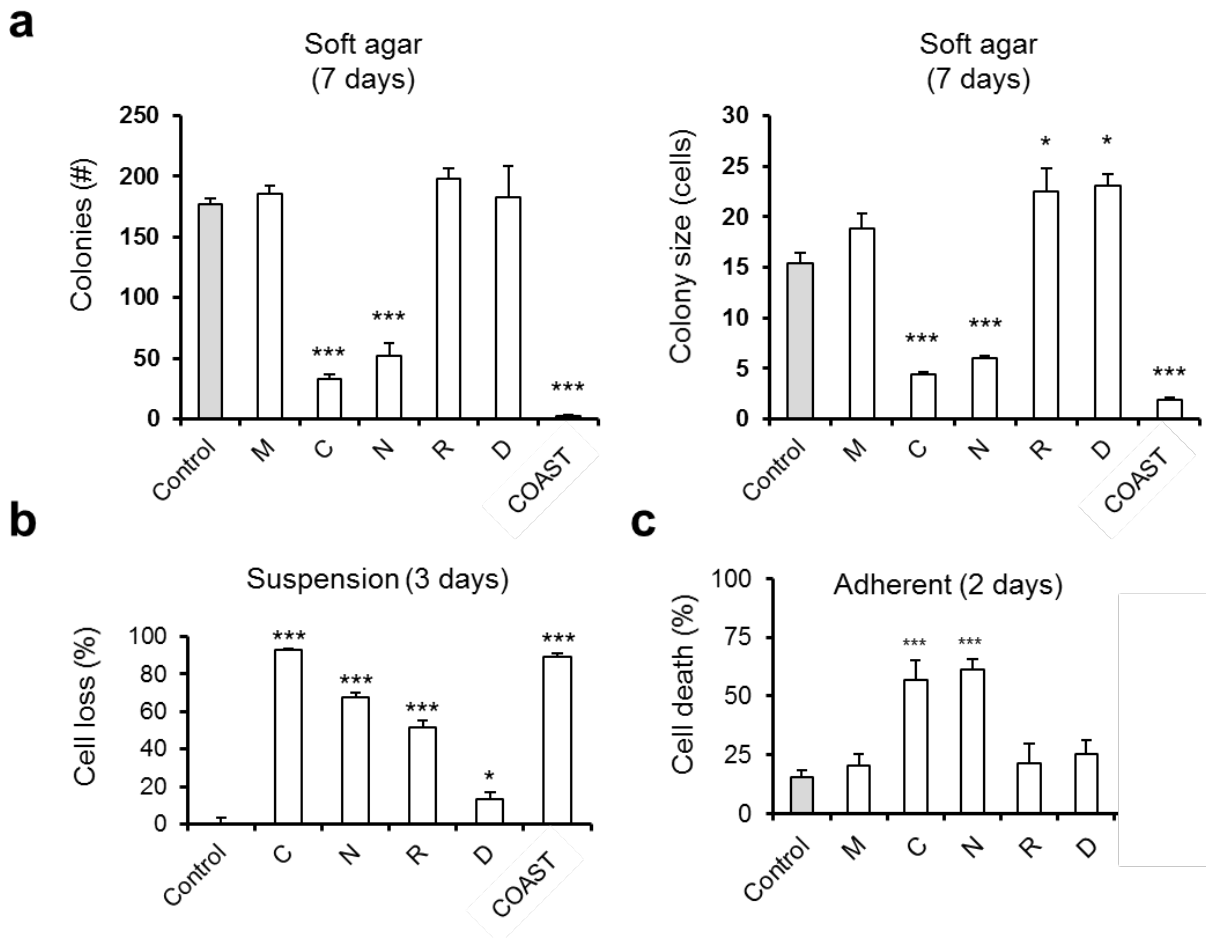
**Supplementary Figure 9. Bortezomib is cytotoxic and induces aggregates, but at the cost of clinical safety.** (a) Crystal violet viability assay of cells treated with indicated concentrations of bortezomib for 48 hours. (b) Immunofluorescence of OVCAR3 cells treated with bortezomib (40nM) and/or COAST (the combination of metformin, chloroquine, nelfinavir, rapamycin, and dasatinib at 10 $\mu$ M, 10 $\mu$ M, 10 $\mu$ M, 10nM, and 50nM, respectively) for 24 hours. Scale bar is 20 $\mu$ m. (c) Safety data from clinical trials suggest non-overlapping toxicity and low toxicity for all COAST drugs used here, with the exception of bortezomib. Due to the high expectation of toxicity with bortezomib, especially in combination, we did not include the drug in further analyses.



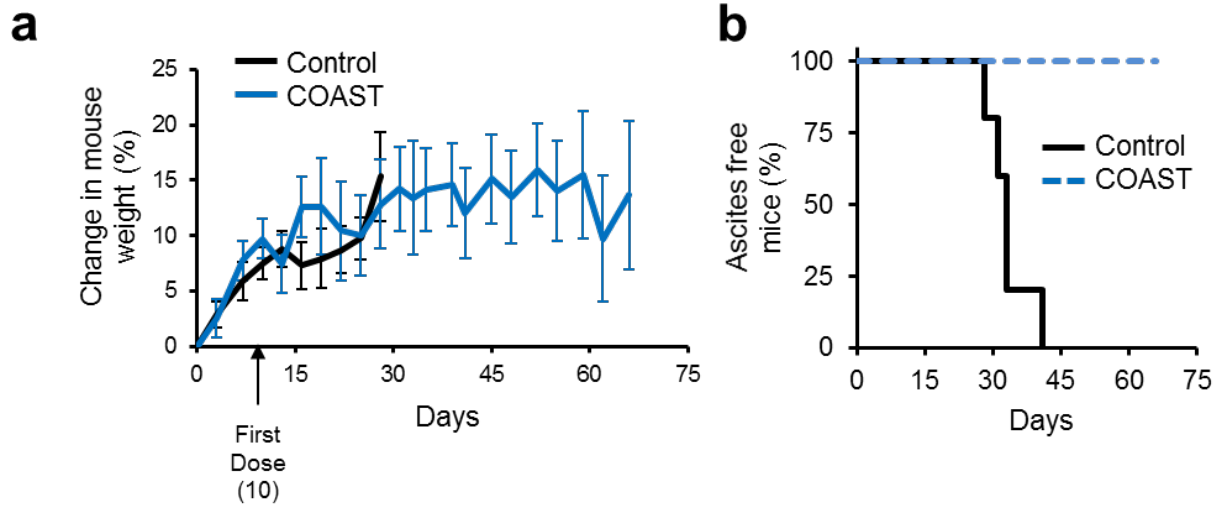
**Supplementary Figure 10. Ovarian cancer cell lines are sensitive to autophagic drugs at physiological levels.** Five human ovarian cancer cell lines (OVs and IGROV1) (note that IGROV1 is unlikely to be serous OV), one low passage patient-derived ovarian cancer (LPPDOV), a mouse ovarian cancer (ID8-IP) and other cancer types are tested for their response to metformin (M), chloroquine (C), nelfinavir (N), rapamycin (R), and dasatinib (D) as well as the common chemotherapeutics cisplatin and docetaxel for reference. Control U373 glioblastoma cells exhibit much less proteotoxic death than any other cancer line. Other cancer types: colorectal (HT29, HCT116), melanoma (M21), lung (A549), and breast (MCF7, MDA-MB-231). Growth is measured by a 48 hour crystal violet assay. Peak blood concentration of drug is indicated in italics. Here, the combination of M,C,N,R, and D at 10μM, 10μM, 10μM, 10nM, and 50nM, is used as COAST, respectively. Mean data from three independent experiments are shown.



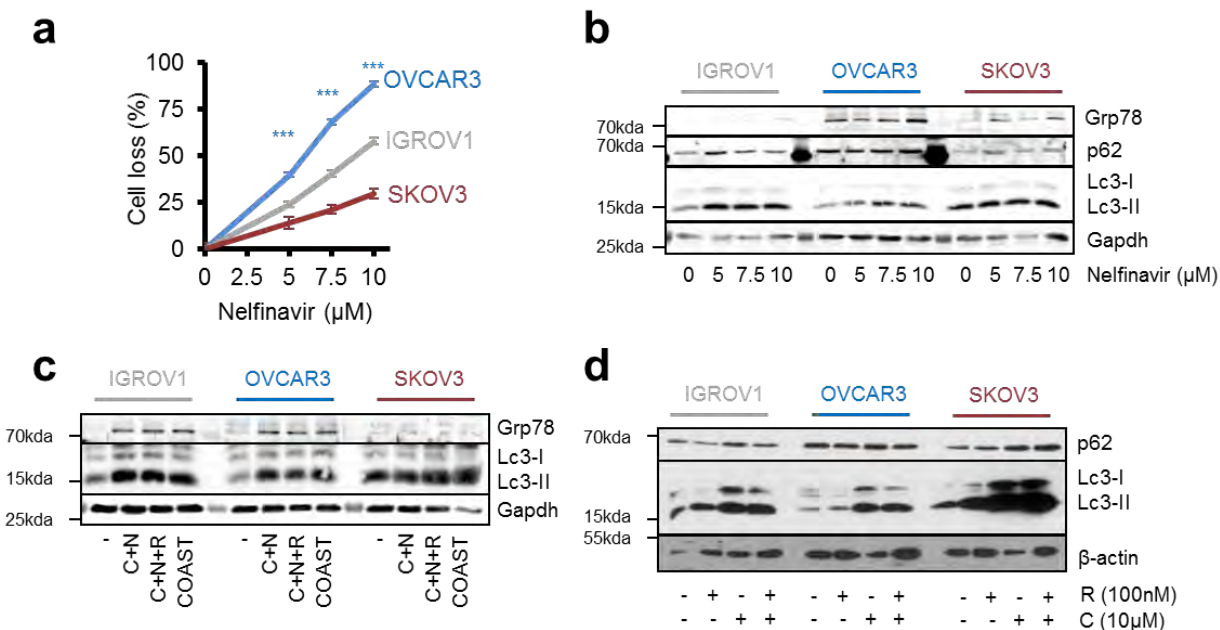
**Supplementary Figure 11. Fully combinatorial autophagy drug studies indicate COAST is more effective than single drugs.** (a) Crystal violet proliferation assays were performed in OVCAR3,5,8,10 cells (grey bars, in order) and autophagy competent (see Supplementary Figure 14) IGROV1 and U373 cells (yellow bars, in order). Each panel shows N-1 drug combinations on the x-axis, with the added drug growth inhibition indicated by the color bars superimposed behind the growth inhibition of the drug indicated on the x-axis. Higher colored bars indicate additivity of the tested drug as compared to a lower order combination. CP indicates cisplatin, at 10 $\mu$ M. Other drugs are at standard COAST concentrations (metformin, M, 10 $\mu$ M, chloroquine, C, 10 $\mu$ M, nelfinavir, N, 10 $\mu$ M, rapamycin, R, 10nM, and/or dasatinib, D, 50nM). Data are from eleven independent experiments, with mean values shown. (b) Specificity of drugs and combinations determined from the data in (a); the average of autophagy competent (U373 and IGROV1) lines' growth inhibition is subtracted from the average of autophagy deficient lines' growth inhibition. Mean values  $\pm$  s.e.m. shown. (c) Drug landscape specificity indicates Log<sub>2</sub> percent increases in cell loss averaged across 17 drug combinations containing the indicated drug when compared to *de-facto* resistant cell line U373. All OVs tested with the exception of IGROV1 show increased sensitivity to COAST drug combinations.



**Supplementary Figure 12. Cytotoxicity of COAST drugs in colony formation and suspension.** (a) OVCAR3 cells were embedded in soft agar and allowed to proliferate for 7 days following treatment with the indicated drugs (COAST component drugs which included metformin (M, 10 $\mu$ M), chloroquine (C, 10 $\mu$ M), nelfinavir (N, 10 $\mu$ M), rapamycin (R, 10nM), and/or dasatinib (D, 50nM), COAST is the five drug combination). Experiment was performed three times with a representative mean $\pm$ s.e.m. shown, \* $p$ <0.05, \*\*\* $p$ <0.001 by two-tailed student's t-test. (b) OVCAR3 cells were grown in polyHEMA plates to force cells into a non-adherent state and tested for drug sensitivity as in (a) for 72 hours of growth. Trypan blue was used to measure cell viability and a ViCell cell counter was used to measure cell counts. Experiment was performed three times with combined mean $\pm$ s.e.m. shown, \* $p$ <0.05, \*\*\* $p$ <0.001 by two-tailed student's t-test. (c) PI staining as a proxy of cell death of adherently grown OVCAR3 cells treated with the indicated drugs for 48 hours, as measured by flow cytometry. Experiment was performed three times with combined mean $\pm$ s.e.m. shown, \*\*\* $p$ <0.001 by two-tailed student's t-test.

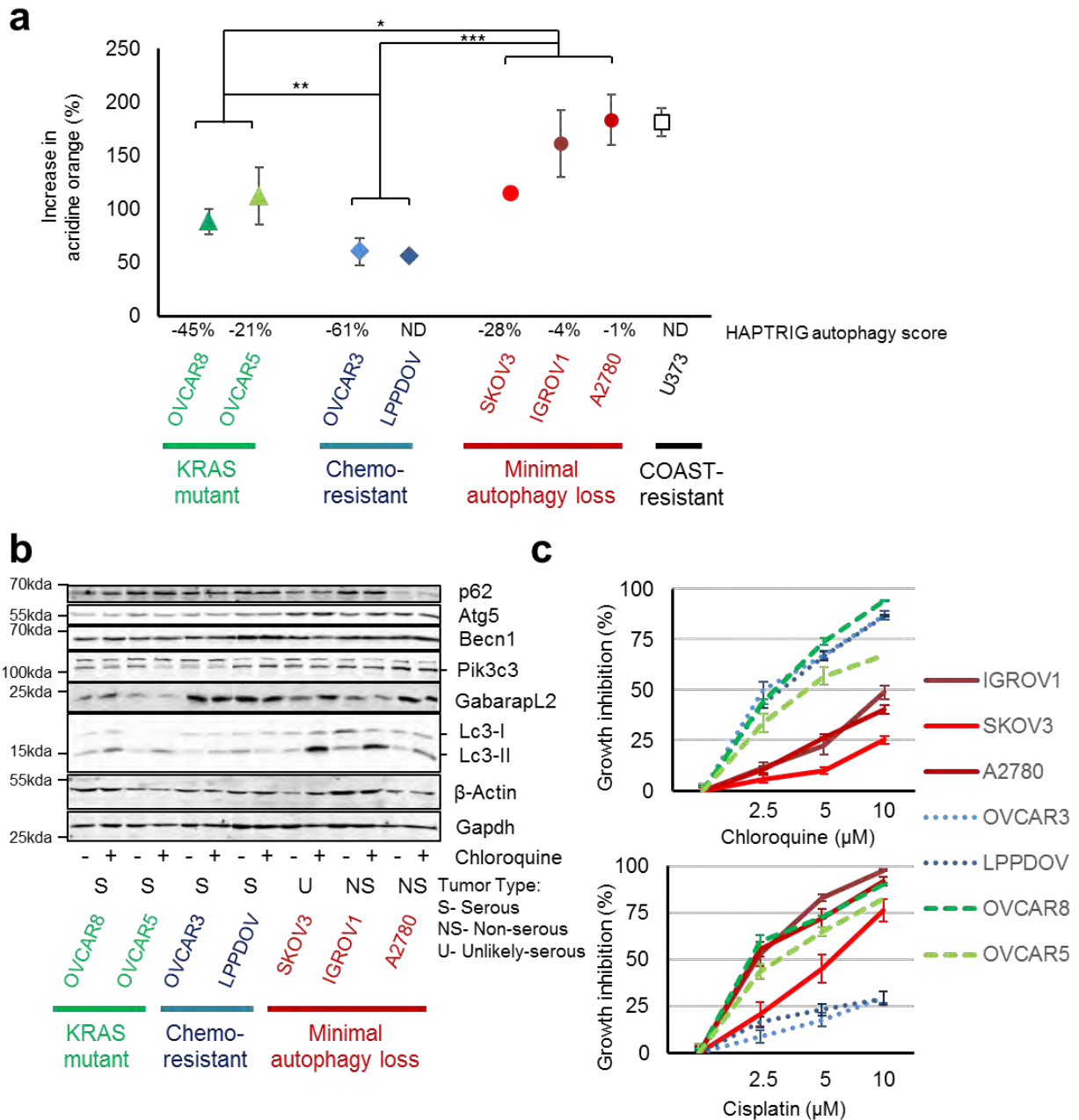


**Supplementary Figure 13. Longer term COAST therapy does not yield weight loss systemic toxicity.** C57BL/6 mice were inoculated IP with ID8-IP tumors and then treated by gavage with COAST identically as in Fig. 4, except for 8 weeks rather than 2 weeks. The mice never lost weight during the course of therapy (a), even long after all control mice were euthanized due to ascites-induced morbidity (b).

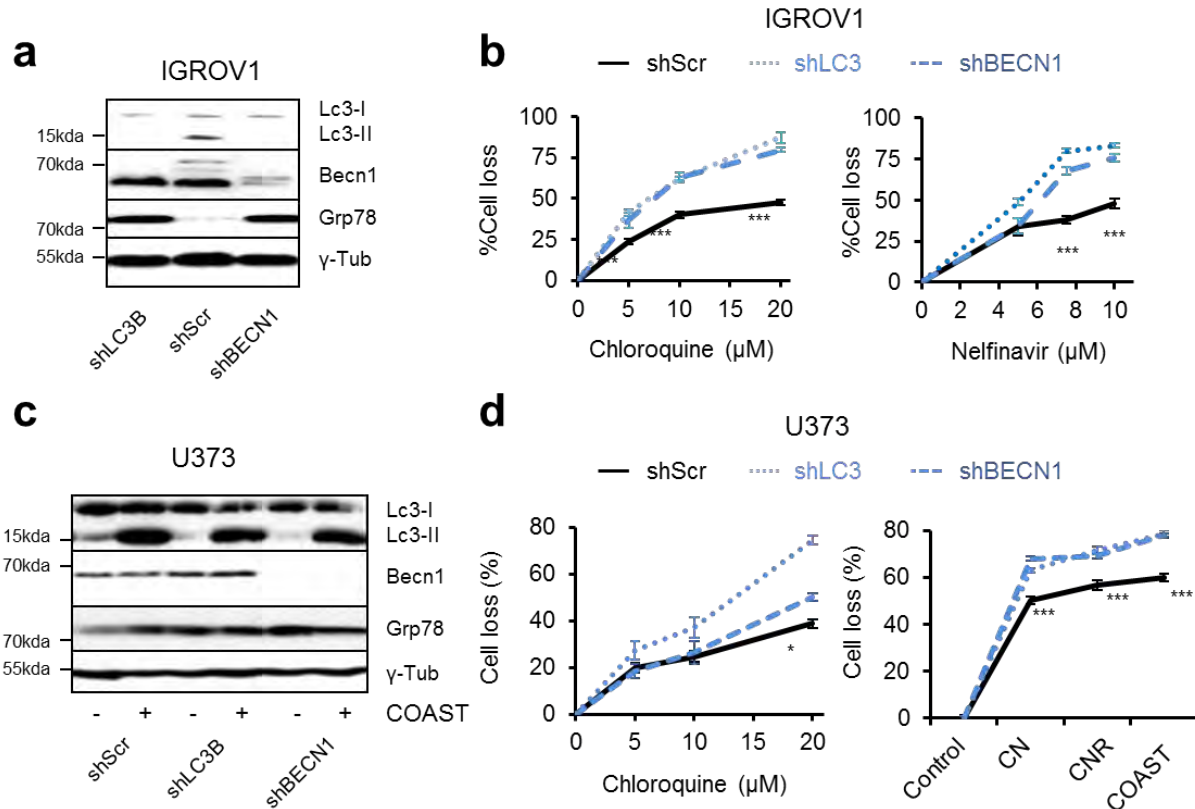


**Supplementary Figure 14. Inadequate autophagy in OVCAR3 following nelfinavir drug treatment.**

(a) Crystal violet viability assay after 48 hours of nelfinavir treatment. Data represent the mean  $\pm$  s.e.m. from eight independent experiments.  $***p < 0.001$  by two-tailed student's t-test, comparing OVCAR3 to either IGROV1 or SKOV3 (all are  $***$ ). (b-d) Western blots of autophagosomal Lc3-II indicate reduced accumulation of autophagosomes in OVCAR3 and increased levels of ER-stress marker Grp78 when treated with nelfinavir (b), combinations of drugs (c) including chloroquine (10 $\mu$ M, C), nelfinavir (10 $\mu$ M, N), rapamycin (R, 10nM), or more (COAST, which additionally includes metformin 10 $\mu$ M and dasatinib 50nM), or with combinations of the autophagy activator rapamycin with the autophagy clearance inhibitor chloroquine (d). Lysates were generated 24h after initiation of treatment. Lysates from three independent experiments were analyzed and a representative blot is shown.



**Supplementary Figure 15. Additional OV cell lines tested for autophagy.** Related to Fig. 4. (a) OVCAR3 and LPPDOV have delayed accumulation of acidic vacuoles including autophagosomes and lysosomes, as measured by acridine orange flow cytometry, when treated with the autophagy/lysosome inhibitor chloroquine (10 $\mu$ M, 24h). *KRAS* mutant but autophagy gene-deleted OVCAR8 and OVCAR5 have somewhat less of a delay, compared to cell lines with less core autophagy gene deletions: SKOV3, IGROV1, and A2780. HAPTRIG autophagy pathway scores are shown for comparison, when data are available (if not, then "ND"). Data represent the mean  $\pm$  s.e.m. from three independent experiments. (b) Western blots of autophagosomal Lc3-II and other autophagy genes for the cell lines tested throughout this paper. Lysates from three independent experiments were analyzed and a representative blot is shown. Chloroquine treatment was 24h. (c) Crystal violet 48h cell death assays are shown for all cell lines for comparison. Of note, cisplatin resistance is not associated with chloroquine resistance.



**Supplementary Figure 16. LC3 and BECN1 gene suppression sensitizes IGROV1 and U373 cells to COAST.** (a) IGROV1, a non-serous and autophagy competent ovarian cancer, was stably knocked down for the genes *LC3* and *BECN1*. Moderate knockdown clones (n=2) were selected for subsequent tests as a haploinsufficient mimetic. Lysates from three independent experiments were analyzed and a representative blot is shown. (b) Proliferation assays of IGROV1 knockdown cells in the presence of the COAST drugs chloroquine or nelfinavir. Data represent the mean  $\pm$  s.e.m. from five independent experiments. \*\*\*p<0.001 by two-tailed student's t-test, indicating shScr is less sensitive than both shBECN1 and shLC3. (c) U373, a cell line found to be resistant to COAST drugs, was stably knocked down for the genes *LC3* and *BECN1*. Lysates from three independent experiments were analyzed and a representative blot is shown. (d) Proliferation assays of U373 knockdown cells in the presence chloroquine of COAST drug combinations (C, Chloroquine 10μM, N, Nelfinavir 10μM, R, Rapamycin 10nM, COAST is CNR plus 10μM metformin and 50nM dasatinib). Data represent the mean  $\pm$  s.e.m. from three independent experiments. \*p<0.05, \*\*\*p<0.001 by two-tailed student's t-test, indicating shScr is less sensitive than both shBECN1 and shLC3.

Fig. 4d

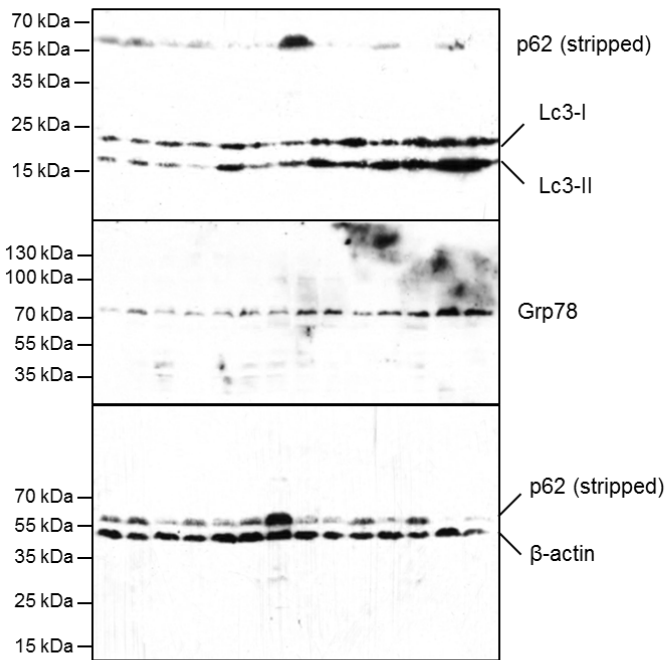


Fig. 5d

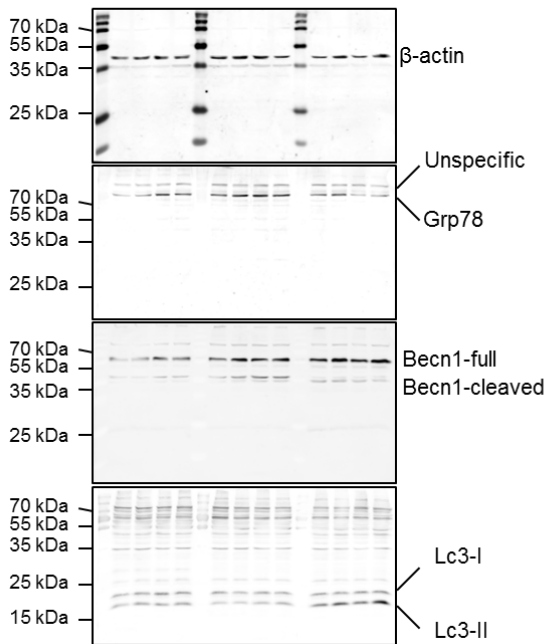
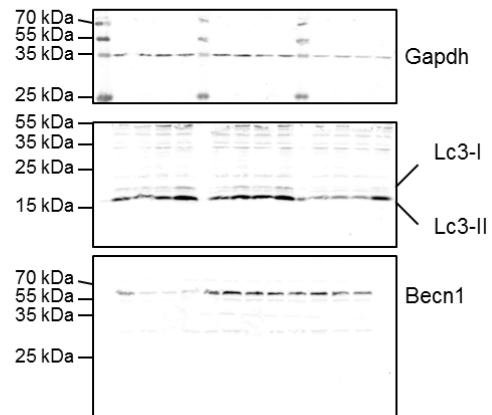


Fig. 5f



Supplementary Figure 17. Uncropped western blots.

Pathway	HAPTRIG Rank (-)	HAPTRIG Rank (+)	HAPTRIG Result	HAPTRIG p value	HAPTRIG q value	GSEA Rank (-)	GSEA Rank (+)	Rank difference	GSEA NES	GSEA p-val	GSEA q-val
Autophagy	1		Haploinsufficient	6.13E-73	1.15E-70	10		-9	-1.45	ns	ns
FoxO signaling pathway	2		Haploinsufficient	4.5E-70	8.42E-68	15		-13	-1.33	ns	ns
Arginine and proline metabolism	3		Haploinsufficient	8.57E-70	1.60E-67	11		-8	-1.41	ns	ns
Adipocytokine signaling pathway	4		Haploinsufficient	2.45E-66	4.58E-64	2		2	-1.88	0.002	ns
Notch signaling pathway	5		Haploinsufficient	1.33E-63	2.49E-61	54		-49	-1.00	ns	ns
Longevity regulating pathway	6		Haploinsufficient	1.74E-48	3.25E-46	28		-22	-1.16	ns	ns
Fatty acid degradation	7		Haploinsufficient	1.05E-44	1.96E-42	1		6	-2.05	0	0.004
AMPK signaling pathway	8		Haploinsufficient	1.36E-43	2.54E-41	19		-11	-1.27	ns	ns
Ubiquitin mediated proteolysis	9		Haploinsufficient	4.48E-41	8.38E-39	42		-33	-1.07	ns	ns
Neuroactive ligand receptor interaction	10		Haploinsufficient	5.49E-39	1.03E-36	22		-12	-1.26	ns	ns
Retinol metabolism	11		Haploinsufficient	5.69E-39	1.06E-36	6		5	-1.62	0.031	ns
Huntington disease	12		Haploinsufficient	1.83E-36	3.42E-34	23		-11	-1.23	ns	ns
Glycolysis Gluconeogenesis	13		Haploinsufficient	2.1E-36	3.93E-34	3		10	-1.73	0.01	ns
HIF1 signaling pathway	14		Haploinsufficient	9.13E-35	1.71E-32	9		5	-1.54	0.019	ns
Lysosome	15		Haploinsufficient	7.46E-34	1.40E-31	13		2	-1.38	0.05	ns
Non small cell lung cancer	16		Haploinsufficient	4.48E-33	1.37E-30		38	NA	0.96	ns	ns
Thyroid hormone signaling pathway	17		Haploinsufficient	5.53E-31	1.03E-28	31		-14	-1.14	ns	ns
Fanconi anemia pathway	18		Haploinsufficient	2.58E-30	4.82E-28	30		-12	-1.15	ns	ns
Epstein Barr virus infection	19		Haploinsufficient	8.01E-30	1.50E-27	39		-20	-1.07	ns	ns
Renal cell carcinoma	20		Haploinsufficient	5.13E-27	9.59E-25	40		-20	-1.07	ns	ns
Glucagon signaling pathway	21		Haploinsufficient	4.25E-26	7.95E-24	48		-27	-1.04	ns	ns
Chronic myeloid leukemia	22		Haploinsufficient	9.42E-26	1.76E-23		36	NA	0.99	ns	ns
Viral myocarditis	23		Haploinsufficient	1.36E-24	2.54E-22	68		-45	-0.93	ns	ns
p53 signaling pathway	24		Haploinsufficient	2.46E-24	4.60E-22	50		-26	-1.01	ns	ns
Protein processing in endoplasmic reticulum	25		Haploinsufficient	5.62E-24	1.05E-21	58		-33	-0.96	ns	ns
Viral carcinogenesis	26		Haploinsufficient	6.8E-23	1.27E-20	41		-15	-1.07	ns	ns
Biosynthesis of amino acids	27		Haploinsufficient	1.31E-22	2.45E-20	59		-32	-0.95	ns	ns
Transcriptional misregulation in cancer	28		Haploinsufficient	2.17E-22	4.06E-20	61		-33	-0.94	ns	ns
mTOR signaling pathway	29		Haploinsufficient	4.23E-22	7.91E-20	27		2	-1.19	ns	ns
Insulin secretion	30		Haploinsufficient	7.79E-22	1.46E-19	84		-54	-0.84	ns	ns
TNF signaling pathway	31		Haploinsufficient	1.07E-20	2.00E-18	34		-3	-1.12	ns	ns
AGE RAGE signaling pathway in diabetic complications	32		Haploinsufficient	1.27E-20	2.37E-18	33		-1	-1.13	ns	ns
Cytokine cytokine receptor interaction	33		Haploinsufficient	8.96E-20	1.68E-17	4		29	-1.64	0.001	ns
Apoptosis	34		Haploinsufficient	1.1E-19	2.06E-17	95		-61	-0.81	ns	ns
Herpes simplex infection	35		Haploinsufficient	1.96E-19	3.67E-17	80		-45	-0.87	ns	ns
RNA degradation	36		Haploinsufficient	3.84E-19	7.18E-17	20		16	-1.26	ns	ns
Starch and sucrose metabolism	37		Haploinsufficient	1.34E-18	2.51E-16	17		20	-1.29	ns	ns
PPAR signaling pathway	38		Haploinsufficient	1.88E-18	3.52E-16	102		-64	-0.77	ns	ns
Endometrial cancer	39		Haploinsufficient	2E-18	3.74E-16	94		-55	-0.81	ns	ns
Basal transcription factors	40		Haploinsufficient	3E-18	5.61E-16	92		-52	-0.82	ns	ns
Inositol phosphate metabolism	41		Haploinsufficient	3.74E-18	6.99E-16	43		-2	-1.07	ns	ns
Pancreatic cancer	42		Haploinsufficient	8.04E-18	1.50E-15	118		-76	-0.63	ns	ns
Fc epsilon RI signaling pathway	43		Haploinsufficient	1.08E-17	2.02E-15	99		-56	-0.80	ns	ns
Acute myeloid leukemia	44		Haploinsufficient	1.47E-17	2.75E-15	122		-78	-0.58	ns	ns
Vasopressin-regulated water reabsorption	45		Haploinsufficient	3.08E-17	5.76E-15	21		24	-1.26	ns	ns
NF kappa B signaling pathway	46		Haploinsufficient	4.48E-17	8.38E-15	93		-47	-0.82	ns	ns
Alcoholism	47		Haploinsufficient	5.31E-17	9.93E-15	91		-44	-0.82	ns	ns
Pantothenate and CoA biosynthesis	48		Haploinsufficient	5.41E-17	1.01E-14	83		-35	-0.85	ns	ns
Oxidative phosphorylation	49		Haploinsufficient	1.08E-16	2.02E-14	88		-39	-0.82	ns	ns
Phagosome	50		Haploinsufficient	1.58E-16	2.95E-14	116		-66	-0.65	ns	ns
SNARE interactions in vesicular transport	51		Haploinsufficient	2.17E-16	4.06E-14	37		14	-1.10	ns	ns
Colorectal cancer	52		Haploinsufficient	3.48E-16	6.51E-14	82		-30	-0.86	ns	ns
Toll like receptor signaling pathway	53		Haploinsufficient	1.43E-15	2.67E-13	98		-45	-0.81	ns	ns
RIG I like receptor signaling pathway	54		Haploinsufficient	4.32E-15	8.08E-13	56		-2	-0.98	ns	ns
Purine metabolism	55		Haploinsufficient	1.37E-14	2.56E-12	55		0	-0.99	ns	ns
Influenza A	56		Haploinsufficient	1.39E-14	2.60E-12	121		-65	-0.59	ns	ns
Metabolism of xenobiotics by cytochrome P450	57		Haploinsufficient	1.09E-09	2.04E-07	7		50	-1.57	0.027	ns
Chemical carcinogenesis	58		Haploinsufficient	2.27E-09	4.24E-07	5		53	-1.62	0.015	ns
Glycerophospholipid metabolism		1	Triploproficient	1.81E-63	3.38E-61		19	-18	1.18	ns	ns
Glycerolipid metabolism	2		Triploproficient	1.12E-58	2.09E-56		3	-1	1.64	0.018	ns
ECM receptor interaction	3		Triploproficient	2.13E-56	3.98E-54		4	-1	1.63	0.023	ns
Oxytocin signaling pathway	4		Triploproficient	1.42E-51	2.66E-49		7	-3	1.43	0.03	ns
Complement and coagulation cascades	5		Triploproficient	2.71E-47	5.07E-45		1	4	2.03	0	0.022
Small cell lung cancer	6		Triploproficient	5.3E-46	9.91E-44		6	0	1.60	0.021	ns
Focal adhesion	7		Triploproficient	1.73E-32	3.24E-30		23	-16	1.12	ns	ns
Wnt signaling pathway	8		Triploproficient	8.35E-32	1.56E-29	51		NA	-1.01	ns	ns
RNA transport	9		Triploproficient	3.41E-29	6.38E-27		29	-20	1.02	ns	ns
N-Glycan biosynthesis	10		Triploproficient	6.61E-29	1.24E-26		26	-16	1.07	ns	ns
Hippo signaling pathway	11		Triploproficient	1.42E-28	2.66E-26		45	-34	0.91	ns	ns
Cell adhesion molecules (CAMs)	12		Triploproficient	2.04E-28	3.81E-26		5	7	1.62	0.006	ns
MAPK signaling pathway	13		Triploproficient	3.13E-28	5.85E-26	75		NA	-0.89	ns	ns
Platelet activation	14		Triploproficient	3.6E-28	6.73E-26		9	5	1.34	ns	ns
Lysine degradation	15		Triploproficient	9.43E-28	1.76E-25		22	-7	1.13	ns	ns
Vascular smooth muscle contraction	16		Triploproficient	3.01E-27	5.63E-25		13	3	1.27	ns	ns
Peroxisome	17		Triploproficient	3.51E-27	6.56E-25		37	-20	0.98	ns	ns
Prolactin signaling pathway	18		Triploproficient	5.81E-27	1.09E-24		44	-26	0.91	ns	ns
Cell cycle	19		Triploproficient	3.94E-26	7.37E-24	70		NA	-0.91	ns	ns

Serotonergic synapse	20	Triploproficient	4.85E-26	9.07E-24		16	4	1.22	ns	ns	
Pancreatic secretion	21	Triploproficient	9.67E-26	1.81E-23		15	6	1.23	ns	ns	
Signaling pathways regulating pluripotency of stem cells	22	Triploproficient	1.74E-25	3.25E-23	110		NA	-0.71	ns	ns	
Central carbon metabolism in cancer	23	Triploproficient	5.18E-25	9.69E-23	114		NA	-0.67	ns	ns	
Dilated cardiomyopathy	24	Triploproficient	2.02E-24	3.78E-22		20	4	1.16	ns	ns	
PI3K Akt signaling pathway	25	Triploproficient	2.09E-24	3.91E-22	71		NA	-0.91	ns	ns	
Melanogenesis	26	Triploproficient	4E-24	7.48E-22	74		NA	-0.89	ns	ns	
Gastric acid secretion	27	Triploproficient	5.17E-24	9.67E-22		21	6	1.14	ns	ns	
Ribosome biogenesis in eukaryotes	28	Triploproficient	1.64E-22	3.07E-20	72		NA	-0.91	ns	ns	
mRNA surveillance pathway	29	Triploproficient	1.84E-22	3.44E-20		11	18	1.33	ns	ns	
Glycosylphosphatidylinositol (GPI) anchor biosynthesis	30	Triploproficient	1.94E-22	3.63E-20		24	6	1.11	ns	ns	
Morphine addiction	31	Triploproficient	1.42E-21	2.66E-19		51	-20	0.83	ns	ns	
Circadian entrainment	32	Triploproficient	1.42E-21	2.66E-19	73		NA	-0.89	ns	ns	
Spliceosome	33	Triploproficient	2.17E-21	4.06E-19		31	2	1.02	ns	ns	
Fc gamma R-mediated phagocytosis	34	Triploproficient	2.24E-21	4.19E-19		48	-14	0.88	ns	ns	
Hypertrophic cardiomyopathy (HCM)	35	Triploproficient	1.06E-20	1.98E-18		18	17	1.19	ns	ns	
Hepatitis B	36	Triploproficient	2.15E-20	4.02E-18		61	-25	0.69	ns	ns	
Regulation of actin cytoskeleton	37	Triploproficient	2.27E-20	4.24E-18		89		NA	-0.82	ns	ns
Insulin resistance	38	Triploproficient	9.69E-20	1.81E-17	49		NA	-1.02	ns	ns	
Adrenergic signaling in cardiomyocytes	39	Triploproficient	9.87E-20	1.85E-17		17	22	1.21	ns	ns	
Cholinergic synapse	40	Triploproficient	1.81E-19	3.38E-17		40	0	0.95	ns	ns	
Axon guidance	41	Triploproficient	2.25E-19	4.21E-17		10	31	1.34	ns	ns	
Prostate cancer	42	Triploproficient	2.58E-19	4.82E-17	66		NA	-0.93	ns	ns	
Arrhythmogenic right ventricular cardiomyopathy (ARVC)	43	Triploproficient	3.23E-19	6.04E-17		27	16	1.05	ns	ns	
Retrograde endocannabinoid signaling	44	Triploproficient	2.43E-18	4.54E-16		28	16	1.03	ns	ns	
Shigellosis	45	Triploproficient	3.01E-18	5.63E-16		50	-5	0.85	ns	ns	
Basal cell carcinoma	46	Triploproficient	1.22E-17	2.28E-15	57		NA	-0.96	ns	ns	
GABAergic synapse	47	Triploproficient	2.23E-17	4.17E-15	109		NA	-0.72	ns	ns	
Chemokine signaling pathway	48	Triploproficient	2.7E-17	5.05E-15	8		NA	-1.56	0.007	ns	
Gap junction	49	Triploproficient	3.26E-17	6.10E-15	26		NA	-1.19	ns	ns	
Dopaminergic synapse	50	Triploproficient	3.43E-17	6.41E-15		47	3	0.90	ns	ns	
HTLV-I infection	51	Triploproficient	9.94E-17	1.86E-14	60		NA	-0.94	ns	ns	
Renin secretion	52	Triploproficient	3.42E-16	6.40E-14		12	40	1.30	ns	ns	
Bacterial invasion of epithelial cells	53	Triploproficient	4.79E-16	8.96E-14	29		NA	-1.15	ns	ns	
Bladder cancer	54	Triploproficient	1.75E-15	3.27E-13		34	20	1.01	ns	ns	
Salivary secretion	55	Triploproficient	2.89E-15	5.40E-13		57	-2	0.75	ns	ns	
cGMP PKG signaling pathway	56	Triploproficient	3.07E-15	5.74E-13		39	17	0.95	ns	ns	
Malaria	57	Triploproficient	3.26E-15	6.10E-13	113		NA	-0.69	ns	ns	
Proteoglycans in cancer	58	Triploproficient	3.33E-15	6.23E-13	87		NA	-0.82	ns	ns	
Rap1 signaling pathway	59	Triploproficient	4.26E-15	7.97E-13	96		NA	-0.81	ns	ns	
Pathogenic Escherichia coli infection	60	Triploproficient	7.03E-15	1.31E-12		8	52	1.40	ns	ns	
Insulin signaling pathway	61	Triploproficient	1.44E-14	2.69E-12	85		NA	-0.84	ns	ns	
Salmonella infection	62	Triploproficient	2.48E-14	4.64E-12		60	2	0.71	ns	ns	
Oocyte meiosis	63	Triploproficient	2.81E-14	5.25E-12		56	7	0.75	ns	ns	
Neurotrophin signaling pathway	64	Triploproficient	3.42E-14	6.40E-12	47		NA	-1.04	ns	ns	
MicroRNAs in cancer	65	Triploproficient	4.76E-14	8.90E-12	24		NA	-1.23	ns	ns	
ErbB signaling pathway	66	Triploproficient	5.28E-14	9.87E-12		46	20	0.90	ns	ns	
Long-term depression	67	Triploproficient	5.8E-14	1.08E-11	35		NA	-1.11	ns	ns	
Adherens junction	68	Triploproficient	5.91E-14	1.11E-11	106		NA	-0.75	ns	ns	
Parkinson disease	69	Triploproficient	8.08E-14	1.51E-11	77		NA	-0.88	ns	ns	
Estrogen signaling pathway	70	Triploproficient	8.1E-14	1.51E-11		30	40	1.02	ns	ns	
Aldosterone synthesis and secretion	71	Triploproficient	8.11E-14	1.52E-11		49	22	0.85	ns	ns	
Leukocyte transendothelial migration	72	Triploproficient	8.49E-14	1.59E-11	97		NA	-0.81	ns	ns	
Glioma	73	Triploproficient	9.35E-14	1.75E-11	69		NA	-0.92	ns	ns	
Amoebiasis	74	Triploproficient	1.11E-13	2.08E-11	67		NA	-0.93	ns	ns	
Natural killer cell mediated cytotoxicity	75	Triploproficient	1.49E-13	2.79E-11	117		NA	-0.64	ns	ns	
Regulation of lipolysis in adipocytes	76	Triploproficient	1.6E-13	2.99E-11		58	18	0.74	ns	ns	
Inflammatory mediator regulation of TRP channels	77	Triploproficient	1.68E-13	3.14E-11	32		NA	-1.14	ns	ns	
Alzheimer disease	78	Triploproficient	4.15E-13	7.76E-11		33	45	1.01	ns	ns	
Phosphatidylinositol signaling system	79	Triploproficient	5.59E-13	1.05E-10		25	54	1.10	ns	ns	
Melanoma	80	Triploproficient	7.34E-13	1.37E-10	81		NA	-0.87	ns	ns	
Hedgehog signaling pathway	81	Triploproficient	7.69E-13	1.44E-10		41	40	0.94	ns	ns	
Non alcoholic fatty liver disease (NAFLD)	82	Triploproficient	1.09E-12	2.04E-10	65		NA	-0.93	ns	ns	
Pathways in cancer	83	Triploproficient	1.21E-12	2.26E-10	64		NA	-0.93	ns	ns	
Endocytosis	84	Triploproficient	1.4E-12	2.62E-10	79		NA	-0.87	ns	ns	
cAMP signaling pathway	85	Triploproficient	1.67E-12	3.12E-10	76		NA	-0.88	ns	ns	
Longevity regulating pathway multiple species	86	Triploproficient	2.73E-12	5.11E-10	120		NA	-0.61	ns	ns	
Cardiac muscle contraction	87	Triploproficient	2.76E-12	5.16E-10		43	44	0.92	ns	ns	
TGF beta signaling pathway	88	Triploproficient	4.87E-12	9.11E-10		54	34	0.77	ns	ns	
Legionellosis	89	Triploproficient	4.96E-12	9.28E-10		63	26	0.64	ns	ns	
GnRH signaling pathway	90	Triploproficient	6.08E-12	1.14E-09	36		NA	-1.11	ns	ns	
Choline metabolism in cancer	91	Triploproficient	7.11E-12	1.33E-09	100		NA	-0.79	ns	ns	
Calcium signaling pathway	92	Triploproficient	8.86E-12	1.66E-09	38		NA	-1.08	ns	ns	
Amino sugar and nucleotide sugar metabolism	93	Triploproficient	1.45E-11	2.71E-09	112		NA	-0.70	ns	ns	
Sphingolipid signaling pathway	94	Triploproficient	1.76E-11	3.29E-09	44		NA	-1.06	ns	ns	
ABC transporters	95	Triploproficient	2.07E-11	3.87E-09		42	53	0.93	ns	ns	
Tight junction	96	Triploproficient	3.71E-11	6.94E-09	12		NA	-1.38	ns	ns	
Primary immunodeficiency	97	Triploproficient	4.26E-11	7.97E-09		35	62	0.99	ns	ns	
Hematopoietic cell lineage	98	Triploproficient	3.61E-10	6.75E-08		14	84	1.25	ns	ns	
Olfactory transduction	99	Triploproficient	4.33E-06	8.10E-04		2	97	1.71	0	ns	

Drug metabolism cytochrome P450		No Selection	ns	ns	18		NA	-1.29	ns	ns
Glutathione metabolism		No Selection	ns	ns	16		NA	-1.31	ns	ns
Nucleotide excision repair		No Selection	ns	ns	62		NA	-0.94	ns	ns
Osteoclast differentiation		No Selection	ns	ns		62	NA	0.66	ns	ns
Inflammatory bowel disease (IBD)		No Selection	ns	ns	46		NA	-1.05	ns	ns
Chagas disease (American trypanosomiasis)		No Selection	ns	ns	14		NA	-1.34	ns	ns
Leishmaniasis		No Selection	ns	ns	119		NA	-0.63	ns	ns
Pertussis		No Selection	ns	ns	115		NA	-0.66	ns	ns
Taste transduction		No Selection	ns	ns	52		NA	-1.01	ns	ns
Arachidonic acid metabolism		No Selection	ns	ns	45		NA	-1.05	ns	ns
Progesterone mediated oocyte maturation		No Selection	ns	ns	107		NA	-0.73	ns	ns
NOD like receptor signaling pathway		No Selection	ns	ns	53		NA	-1.00	ns	ns
Jak STAT signaling pathway		No Selection	ns	ns	111		NA	-0.70	ns	ns
Bile secretion		No Selection	ns	ns	104		NA	-0.77	ns	ns
Tuberculosis		No Selection	ns	ns	86		NA	-0.83	ns	ns
Fatty acid metabolism		No Selection	ns	ns	108		NA	-0.72	ns	ns
Thyroid hormone synthesis		No Selection	ns	ns	90		NA	-0.82	ns	ns
Cytosolic DNA-sensing pathway		No Selection	ns	ns		52	NA	0.83	ns	ns
Cocaine addiction		No Selection	ns	ns	105		NA	-0.75	ns	ns
Rheumatoid arthritis		No Selection	ns	ns	78		NA	-0.88	ns	ns
Toxoplasmosis		No Selection	ns	ns		32	NA	1.01	ns	ns
Amphetamine addiction		No Selection	ns	ns		59	NA	0.74	ns	ns
Glutamatergic synapse		No Selection	ns	ns	101		NA	-0.78	ns	ns
Measles		No Selection	ns	ns		64	NA	0.55	ns	ns
B cell receptor signaling pathway		No Selection	ns	ns		55	NA	0.76	ns	ns
Hepatitis C		No Selection	ns	ns	103		NA	-0.77	ns	ns
Phospholipase D signaling pathway		No Selection	ns	ns	63		NA	-0.94	ns	ns
Carbon metabolism		No Selection	ns	ns		65	NA	0.35	ns	ns
Ras signaling pathway		No Selection	ns	ns	25		NA	-1.21	ns	ns
T cell receptor signaling pathway		No Selection	ns	ns		53	NA	0.78	ns	ns

**Supplementary Table 1: Direct comparison of HAPTRIG to GSEA on OV/KEGG analysis**

GSEA was performed using identical parameters as used in HAPTRIG analysis presented here.

For p and q values, "ns" indicates p>0.05.

Autophagy	Low					High				
	1	2	3	4	5	1	2	3	4	5
BLCA	ATG4B	GABARAP	ATG12	ATG16L1	MAP1LC3B	BECN1	ATG3	ATG7	PRKAA1	PIK3R4
BRCA	MAP1LC3B	GABARAPL2	GABARAP	ATG4B	ULK1	PRKAA1	MDM4	WWP1	CLN3	TSC2
CECSC	GABARAP	ATG4B	ATG7	ATG12	MAP1LC3B	ATG3	PRKAA1	PIK3R4	PRKAA2	BECN1
COADREAD	GABARAP	PIK3C3	ATG12	HSP90AA1	ULK2	GABARAPL2	MAP1LC3B	ATG16L1	ATG4B	ATG4A
GBM	MAP1LC3B	GABARAPL2	GABARAP	ATG5	ATG13	ATG4D	PRKAA2	DNAJB1	CASP3	CASP8
HNCS	ATG7	ATG12	ATG4B	GABARAP	ATG10	ATG3	BECN1	GABARAPL1	PRKAA1	PIK3R4
KIRC	ATG7	ATG3	PIK3C3	BECN1	HSP90AA1	ATG12	ATG4B	ULK1	GABARAPL1	GABARAPL2
KIRP	HSPA5	ATG4C	MAP3K5	ULK3	DNAJB1	BECN1	GABARAPL2	GABARAP	MAP1LC3B	ATG3
LAML	GABARAP	ATG12	GABARAPL2	MAP1LC3B	ATG3	PRKAA2	WWP1	INS	DNAJB1	ATG16L2
LGG	PRKAA2	ATG4B	ATG3	ULK1	ATG12	ATG4D	GABARAPL1	CASP8	MAN2B1	ATG16L2
LIHC	GABARAP	MAP1LC3B	GABARAPL2	GABARAPL1	ATG13	BECN1	PRKAA1	ATG12	HSP90AB1	HSPA1A
LUAD	GABARAP	MAP1LC3B	ATG7	GABARAPL2	ATG12	BECN1	PRKAA1	PRKAA2	ULK1	HSP90AB1
LUSC	ATG7	GABARAP	ATG12	MAP1LC3B	GABARAPL2	ATG3	PRKAA1	GABARAPL1	PIK3R4	BECN1
OV	MAP1LC3B	BECN1	GABARAPL2	GABARAP	ATG12	GABARAPL1	ATG3	PRKAA1	PRKAA2	HSP90AB1
PAAD	GABARAP	PIK3C3	ATG7	ATG5	ATG12	ATG4B	MDM4	ATG4A	AGPS	TSC2
PRAD	MAP1LC3B	GABARAPL2	GABARAP	GABARAPL1	ATG5	WWP1	MDM4	ATG16L2	TSC2	IFNG
SARC	MAP1LC3B	GABARAPL2	ATG4B	GABARAP	ATG4A	PRKAA2	PRKAA1	ATG4D	HSP90AA1	DNAJB1
SKCM	MAP1LC3B	GABARAP	GABARAPL2	ATG5	ATG12	PRKAA1	HSPA1A	HSP90AB1	WWP1	MDM4
STAD	GABARAP	MAP1LC3B	ATG12	GABARAPL2	ATG7	PRKAA1	BECN1	HSP90AB1	WWP1	MDM4
THCA	UBE2L3	ATG4B	HSPA5	ATG16L1	ATG5	BECN1	ULK1	ATG12	GABARAPL1	GABARAP
UCEC	MAP1LC3B	GABARAPL2	GABARAP	BECN1	ATG12	PRKAA1	ATG3	PRKAA2	PIK3R4	GABARAPL1

ER Stress	Low					High				
	1	2	3	4	5	1	2	3	4	5
BLCA	PARK2	HSPA8	STUB1	HSPA5	TP53	HSPA6	P4HB	NPLOC4	DNAJB11	NSFL1C
BRCA	HSPA8	FBXO6	TP53	PARK2	HSP90AA1	STUB1	HSPA6	YOD1	NPLOC4	HSPA1A
CECSC	HSPA8	PARK2	TP53	CRYAB	MAPK8	DNAJB11	HSPA6	SEC61A1	HSPA1A	HSPA5
COADREAD	HSP90AA1	TP53	PARK2	FBXO6	LMAN1	HSPH1	HSP90AB1	UBE2D4	STUB1	HSPA1A
GBM	HSP90AA1	MAPK8	PARK2	HSPA8	STUB1	UBE2D4	DNAJB1	SMURF1	OS9	SEC61G
HNCS	HSPA8	CRYAB	MAPK9	MAPK8	FBXO6	HSPA5	HSP90AA1	DNAJB11	SEC61A1	HSPA6
KIRC	HSP90AA1	HSPA5	PARK2	FBXO6	HSPA1A	MAPK9	SEC24A	STUB1	UBE2D4	UBE2D2
KIRP	HSP90AA1	HSPA8	PARK2	UBE4B	MAP2K7	STUB1	TP53	P4HB	NPLOC4	AMFR
LAML	TP53	SEC24A	UBQLN1	STUB1	UBE2D4	HSPA8	FBXO6	CRYAB	HSP90AA1	HYOU1
LGG	HSP90AA1	FBXO6	PARK2	UBE4B	HSPA2	HSPA8	DNAJB1	UBE2D4	SMURF1	PRKCSH
LIHC	HSP90AA1	PARK2	TP53	HSPA8	FBXO6	HSPA1A	HSPA6	HSP90AB1	NPLOC4	YOD1
LUAD	PARK2	HSPA5	TP53	UBQLN1	MAP2K7	HSPA6	HSPA1A	NPLOC4	HSP90AB1	P4HB
LUSC	FBXO6	TP53	HSPA8	STUB1	MAPK9	DNAJB11	HSPA6	SEC61A1	NPLOC4	ERLEC1
OV	PARK2	HSPA5	STUB1	TP53	HSP90AA1	HSPA1A	HSPA6	DNAJB11	DNAJB1	NSFL1C
PAAD	PARK2	HSPA5	TP53	HSPA1A	FBXO6	HSPA6	UBE2D4	RFWD2	YOD1	SEC23A
PRAD	TP53	PARK2	UBE2J1	FBXO6	HSP90AA1	HSPA5	SEC61A1	UBE2D4	SMURF1	UBQLN1
SARC	HSPA8	TP53	MAPK8	CRYAB	HSPH1	HSPA5	UBQLN1	MAP2K7	DNAJB1	HSPA6
SKCM	HSPA8	PARK2	HSPA5	HSP90AA1	MAPK8	HSPA1A	HSP90AB1	HSPA6	HSPA1L	NPLOC4
STAD	PARK2	HSP90AA1	TP53	STUB1	MAP2K7	HSP90AB1	HSPA6	HSPA5	UBE2D4	HSPH1
THCA	HSPA5	ATF4	PARK2	UBQLN1	UBE2L3	HSP90AA1	STUB1	NPLOC4	HSPA6	P4HB
UCEC	HSPA5	HSPA8	TP53	AMFR	UBQLN1	HSPA6	HSPA1A	HSP90AB1	HSP90AA1	DNAJB1

Lysosome	Low					High				
	1	2	3	4	5	1	2	3	4	5
BLCA	CTSD	PSAP	TP53	AP3M1	GGA1	CLTC	GGA3	AP1S1	ATR	SEC61A1
BRCA	FBXO6	AP1G1	AP1B1	GGA1	TP53	GGA2	CLTC	GGA3	CLN3	CTSE
CECSC	CTSD	TP53	PSAP	HSPA8	CLTA	DNAJB11	GGA3	CLTC	ATR	SEC61A1
COADREAD	FBXO6	GGA1	TP53	AP4E1	SORT1	CTSA	AP1S1	NEU1	AP1G1	GGA2
GBM	GGA1	AP3M1	PSAP	CTSD	AP3S2	AP1S1	ATP6V0A4	GUSB	AP1G1	CTSA
HNCS	CTSD	FBXO6	AP3M1	ATG7	PSAP	CLTC	DNAJB11	AP1B1	ATR	AP1S1
KIRC	FBXO6	ATG7	GLB1	NPC2	NEU1	GGA2	CLTC	AP1G1	AP1S1	CLTB
KIRP	AP4E1	AP4S1	GBA	LGMN	AP4B1	CLTC	GGA3	GGA2	AP1G1	CLN3
LAML	AP1S1	AP1G1	TP53	CLTC	ATP6V0A4	GGA1	FBXO6	AP3M2	ATP6V0D2	CTSB
LGG	FBXO6	CTSD	SORT1	PPT1	PSAP	AP1S1	AP1G1	CLTC	ATP6V0A4	AP1M2
LIHC	FBXO6	TP53	CLTA	AP1G1	CTSB	CLTC	GGA3	CTSE	NEU1	CTSA
LUAD	GGA1	TP53	CLTA	MAN2B1	AP3M1	CLTC	GGA3	GGA2	CTSE	CTSA
LUSC	FBXO6	CTSD	TP53	PSAP	AP3M1	CLTC	AP1B1	GGA3	GGA1	M6PR
OV	GGA1	CLTC	AP1G1	CTSD	GGA2	DNAJB11	CTSA	SEC61A1	NEU1	ATR

PAAD	FBXO6	GGA1	CLTC	GGA3	TP53	AP1S1	CTSE	ATP6V0D2	CTSA	SEC61A1
PRAD	FBXO6	AP1G1	CLTC	TP53	AP1B1	ATP6V0D2	ATP6V1H	SEC61A1	ATP6V0A4	UBQLN1
SARC	CTSD	PSAP	AP1G1	TP53	CLTA	GGA3	FBXO6	CLTC	MAN2B1	GBA
SKCM	PSAP	CLTA	AP3M1	CTSD	TP53	CLTC	GGA1	GGA3	AP1S1	CTSA
STAD	GGA1	TP53	GGA2	AP4E1	AP1B1	CTSA	NEU1	AP1S1	ATP6V0D2	SEC61A1
THCA	GGA1	AP1B1	IGF2R	ATM	SORT1	CLTC	GGA3	GGA2	CLN3	MDM2
UCEC	AP1G1	GGA1	TP53	CTSD	AP4E1	CTSA	GGA3	DNAJB11	CTSE	NEU1

Proteasome	Low					High				
	1	2	3	4	5	1	2	3	4	5
BLCA	UBE2D2	PARK2	UBE2D3	UBE2D1	TRAF6	SKP2	UBR5	UBE2W	ANAPC11	TCEB1
BRCA	TP53	UBE2L3	PARK2	UBE2D3	WWP2	STUB1	UBE2I	RFWD2	UBE2W	UBR5
CESC	UBE2D3	PARK2	UBE2K	UBE2D1	TRAF6	RFWD2	SKP2	UBE2W	UBR5	UBE2C
COADREAD	UBE2D3	TP53	NEDD4L	UBE2L3	UBE3A	UBE2W	UBE2D4	UBE2C	UBR5	BIRC7
GBM	UBE2D1	PTEN	PARK2	UBE2L3	HUWE1	SMURF1	UBE2D4	FZR1	UBE2H	UBE2C
HNSC	UBE2D2	UBE2D3	UBE2E1	UBE2D1	UBA1	UBR5	UBE2W	SKP2	TCEB1	UBE2L3
KIRC	UBE2E1	PARK2	VHL	UBE2E2	HSP90AA1	UBE2D2	SKP1	UBE2B	MDM2	FBXW11
KIRP	UBE2L3	UBE4B	NEDD4L	HSP90AA1	SFN	BRCA1	STUB1	MDM2	UBE2I	TP53
LAML	UBE2D2	SKP1	UBE2B	TP53	SMURF1	UBE2W	UBR5	UBE2L3	DBB1	BIRC2
LGG	UBE2D1	UBE2D3	PARK2	UBA1	MDM2	SMURF1	FZR1	UBE2H	UBR5	UBE2D4
LIHC	UBE2D3	TP53	PARK2	HUWE1	UBE2G1	RFWD2	UBE2D2	UBR5	UBE2W	SKP2
LUAD	PARK2	FZR1	TP53	UBE2D2	UBE2D3	SKP2	RFWD2	UBE2W	UBR5	BRCA1
LUSC	UBE2D2	UBE2D3	UBE2D1	SKP1	MAP3K1	SKP2	UBE2L3	UBE2W	UBR5	SMURF1
OV	UBE2D3	FZR1	BRCA1	PARK2	UBE2L3	UBR5	RFWD2	SKP2	UBE2W	UBE2H
PAAD	PARK2	TP53	NEDD4L	UBE2L3	HUWE1	RFWD2	UBE2W	UBR5	UBE2D4	SMURF1
PRAD	TP53	PTEN	PARK2	UBE2L3	BRCA1	UBE2W	UBR5	TCEB1	UBE2D4	SMURF1
SARC	UBE2D1	TP53	XIAP	TRAF6	PTEN	MDM2	SKP2	UBE2D2	UBA1	FZR1
SKCM	UBE2D1	PARK2	UBE2D2	UBE2D3	PTEN	UBE2L3	RFWD2	UBE2W	SMURF1	UBE2H
STAD	UBE2D3	UBE2D2	PARK2	TP53	UBE2L3	UBE2W	UBR5	UBE2D4	UBE2C	SMURF1
THCA	UBE2L3	CHEK2	UBE2D1	ANAPC2	PARK2	UBE2D2	SKP1	RFWD2	STUB1	BRCA1
UCEC	UBE2D3	FZR1	TP53	UBE2D2	NEDD4	RFWD2	UBE2D1	UBE2W	UBR5	UBA1

Peroxisome	Low					High				
	1	2	3	4	5	1	2	3	4	5
BLCA	HSD17B4	ACSL4	CAT	TP53	SLC27A2	PEX19	PEX5	PEX12	PEX13	PEX10
BRCA	PEX14	SLC27A2	AGPS	TP53	HSD17B4	PEX19	PEX5	PEX11B	PEX2	ABCD2
CESC	HSD17B4	ACSL4	PEX7	SOD1	TP53	PEX19	PEX14	ABCD3	PEX5	PEX10
COADREAD	PEX14	HSD17B4	PRDX1	SOD1	ABCD3	PEX5	PEX19	PEX1	NOS2	PEX2
GBM	PEX7	ABCD1	PHYH	PEX14	PEX3	PEX19	PEX5	PEX1	GSTK1	PEX6
HNSC	HSD17B4	ACAA1	SOD1	SCP2	ACOX2	PEX5	PEX19	PEX2	ABCD1	PEX13
KIRC	PEX14	PEX3	ACAA1	PEX7	DHRS4	PEX5	HSD17B4	CAT	PEX19	AGPS
KIRP	PEX14	PEX3	SOD1	PRDX1	ABCD3	PEX5	NOS2	PEX12	ABCD1	AGPS
LAML	PEX5	HSD17B4	PEX1	GSTK1	CAT	PEX2	PEX19	SOD1	PEX14	PEX10
LGG	PEX14	ABCD3	PEX10	PRDX1	SCP2	PEX5	PEX1	GSTK1	CROT	PEX6
LIHC	PEX5	PEX14	SOD1	PEX7	PRDX1	PEX19	PEX11B	PEX26	PEX6	PEX1
LUAD	HSD17B4	PEX7	SLC27A2	ACAA1	SOD1	PEX19	PEX5	PEX12	PEX10	PEX11B
LUSC	HSD17B4	PEX14	ACAA1	SOD1	SCP2	PEX5	PEX19	PEX13	AGPS	EHHADH
OV	NOS2	PEX12	HSD17B4	PEX3	TP53	PEX5	PEX19	AGPS	PEX13	PEX11B
PAAD	PEX14	PEX7	SOD1	PEX3	PRDX1	PEX19	PEX5	PEX11B	PEX2	ABCD2
PRAD	PEX5	PEX14	AGPS	ABCD3	HSD17B4	PEX2	PEX1	PEX6	CYCS	PEX5L
SARC	PEX5	AGPS	ABCD1	ACSL4	TP53	PEX19	PEX14	PEX11B	PEX3	PRDX1
SKCM	PEX7	PEX3	HSD17B4	PHYH	SOD1	PEX19	PEX11B	PEX1	PEX6	PEX26
STAD	HSD17B4	SOD1	SCP2	ACAA1	PRDX1	PEX19	PEX5	PEX2	PEX13	PEX1
THCA	PEX26	SLC25A17	AGPS	SOD1	PEX6	PEX5	PEX19	PEX12	NOS2	HSD17B4
UCEC	HSD17B4	SLC27A2	TP53	NUDT7	NUDT12	PEX19	PEX5	PEX13	PEX11B	ABCD3

Blue= Significant allelic loss in this pathway in this cancer type

Red= Significant allelic gain in this pathway in this cancer type

Numbers indicate rank of most impactful gene, from 1 being most impactful to 5 being the 5th most impactful

### Supplementary Table 2: The most positively and negatively impactful genes within HAPTRIG proteostasis networks

Genes were (scored with 1° interactions with other proteostasis pathways).

Pathways with significantly altered networks within a given cancer type are highlighted.

### GISTIC2 Copy Number Alterations: Autophagy Genes

Cell Line	p53 mut	KRAS mut	BECN1	MAP1LC3B	ATG5	PIK3C3	GABARAPL2	ULK2	GABARAP	ATG10	ATG12	ATG13	ATG7	INS	ATG16L2
OVCAR3	R248Q	-	-1	-1	0	-1	-1	1	-2	0	0	1	0	0	2
OVCAR5	-	G12V	1	1	-1	1	-1	0	-1	0	1	-1	-1	-1	1
OVCAR8	X126_splice	P121H	1	1	-1	0	0	-1	-1	1	1	-1	1	-1	1
SKOV3	-	-	2	0	0	0	0	-1	-1	0	0	0	0	-1	0
IGROV1	Y126C	-	0	0	0	-1	0	0	0	0	0	-1	-1	0	0
A2780	-	-	0	0	0	0	-1	0	0	0	0	0	0	0	0
	GABARAPL1	IFNG	ULK1	ATG14	ULK3	ATG4D	ATG4C	PRKAA2	ATG16L1	ATG4B	ATG3	PIK3R4	PRKAA1	ATG4A	
OVCAR3	-1	0	0	1	-1	0	0	0	0	-1	2	2	1	0	
OVCAR5	-1	1	-1	-1	1	1	0	0	0	-1	-1	1	0	-1	
OVCAR8	0	0	1	1	0	1	1	1	0	0	1	1	1	0	
SKOV3	-2	0	0	0	0	0	0	0	0	0	0	0	0	0	
IGROV1	0	0	0	0	0	0	0	0	0	0	-1	0	0	-1	
A2780	0	0	0	0	0	0	0	0	0	0	0	0	0	0	
	IFNA1	IFNA10	IFNA13	IFNA14	IFNA16	IFNA17	IFNA2	IFNA21	IFNA4	IFNA5	IFNA6	IFNA7	IFNA8		
OVCAR3	1	1	1	1	1	1	1	1	1	1	1	1	1		
OVCAR5	-1	-1	-1	-1	-1	-1	-1	-1	-1	-1	-1	-1	-1		
OVCAR8	0	0	0	0	0	0	0	0	0	0	0	0	0		
SKOV3	-1	-1	-1	-1	-1	-1	-1	-1	-1	-1	-1	-1	-1		
IGROV1	0	0	0	0	0	0	0	0	0	0	0	0	0		
A2780	0	0	0	0	0	0	0	0	0	0	0	0	0		

Unknown Genetics: U373, LPPDOV, OVCAR10

#### Supplementary Table 3: Autophagy gene status of cell lines studied

Gain/loss scores from the Cancer Cell Line Encyclopedia as curated by the cBioPortal were used to determine copy number aberrations. KRAS and TP53 mutations are also shown.

Year	Study PMID	Study Title	Pathway Finding	Gene Findings (+ Regulation)	Gene Findings (- Regulation)	Gene Findings (Mutation)	In Vitro test	In Vivo Test
(Current study)		Haploinsufficiency Networks Identify Targetable Patterns of Allelic Deficiency in Low Mutation Ovarian Cancer	Autophagy	CTSD, PEX5, PCAT1/2, many more	MAP1LC3B, BECN1	N/A	10+ models	3 models
2016	27372738	Integrated Proteogenomic Characterization of Human High-Grade Serous Ovarian Cancer	HR, JAK/STAT, SRF, PDGFRb	N/A	N/A	N/A	N/A	N/A
2015	25888305	A network model for angiogenesis in ovarian cancer	Angiogenesis	NFKB1, ARID3A, SOX5, TFAP2A, NKX2-5, PRRX2	AHR, SPIB, MZF1, BRCA1	N/A	N/A	N/A
2015	25710373	Spatial and Temporal Heterogeneity in High-Grade Serous Ovarian Cancer: A Phylogenetic Analysis	Clonal expansions	2q, 3p, Chr10	NF1	TP53, BRCA1/2, NF1, APC	N/A	N/A
2015	26017449	Whole-genome characterization of chemoresistant ovarian cancer	BRCA, MDR	CCNE1, MDR1, ABCB1	RB1, NF1, RAD51B, PTEN	BRCA1, BRCA2	N/A	N/A
2015	25581432	Gene expression analysis identifies global gene dosage sensitivity in cancer	DNA stability	MYC, CCNE1, PIK3CA, BIRC5	TP53, CDKN2A, RB1, BRCA1, BRCA2, ATM	N/A	N/A	N/A
2014	24448499	Integrated analysis of germline and somatic variants in ovarian cancer	Fanconi Anemia, MAPK, MLL, DNA repair	N/A	BRCA, FANC, ATR, others	NF1, KRAS, others	N/A	N/A
2014	24071852	Pan-cancer patterns of somatic copy number alteration	Whole-genome-duplication	CCND1, EGFR, MYC, ERBB2, CCNE1, MCL1, MDM2, WHSC1L1, TERC, TERT, RMRP	ATM, NOTCH, PPP2RA, PTTG11P, FOXK2, LINC00290, ERRF11, FOXC1	N/A	N/A	N/A
2013	24071851	Emerging landscape of oncogenic signatures across human cancers	Cell cycle, BRCA	MYC, CCNE1	TP53, BRCA	TP53, others	N/A	N/A
2013	23822816	Large-scale integrative network-based analysis identifies common pathways disrupted by copy number alterations across cancers	TGFb, MAPK, MYC	MYC, TRIB1, E2F3, AURKA	NCOR1, PPP2RA, CLU, MAP2K4	N/A	N/A	N/A
2011	21720365	Integrated genomic analyses of ovarian carcinoma	RB, RAS, HR, NOTCH, FOXM1	MYC, CXCL10/11, CXCR3, HMGA2, SOX11, MCM2, PCNA, MUC16, MUC1, SLPI, HOX	MUC1, MUC16	TP53, NF1, BRCA1, BRCA2, RB1, CDK12, CSMD3, FAT3, GABRA6	N/A	N/A
2009	19193619	Integrated genome-wide DNA copy number and expression analysis identifies distinct mechanisms of primary chemoresistance in ovarian carcinomas	Cell cycle, ECM deposition	CCNE1, ERBB2, MUC1, MYC	BRCA1, IGF2R	N/A	N/A	N/A

**Supplementary Table 4: Notable pathway analyses performed for OV.**